



BNL-97291-2012-JA

***THE ROLE OF CLOUD MICROPHYSICS PARAMETERIZATION IN THE
SIMULATION OF MESOSCALE CONVECTIVE SYSTEMS AND ANVIL
CLOUDS IN THE TROPICAL WESTERN PACIFIC***

Van Weverberg, K., Vogelmann, A. M., Lin, W., Luke, E. P., Cialella, A.,
Minnis, P., Khaiyer, M., Boer, E. R., and Jensen, M. P.

*Submitted to
J. Aerosol Science*

Accepted for publication
November 2012

Atmospheric Sciences Division/Environmental Sciences Dept.

Brookhaven National Laboratory

**U.S. Department of Energy
Office of Science**

Notice: This manuscript has been authored by employees of Brookhaven Science Associates, LLC under Contract No. DE-AC02-98CH10886 with the U.S. Department of Energy. The publisher by accepting the manuscript for publication acknowledges that the United States Government retains a non-exclusive, paid-up, irrevocable, world-wide license to publish or reproduce the published form of this manuscript, or allow others to do so, for United States Government purposes.

This preprint is intended for publication in a journal or proceedings. Since changes may be made before publication, it may not be cited or reproduced without the author's permission.

DISCLAIMER

This report was prepared as an account of work sponsored by an agency of the United States Government. Neither the United States Government nor any agency thereof, nor any of their employees, nor any of their contractors, subcontractors, or their employees, makes any warranty, express or implied, or assumes any legal liability or responsibility for the accuracy, completeness, or any third party's use or the results of such use of any information, apparatus, product, or process disclosed, or represents that its use would not infringe privately owned rights. Reference herein to any specific commercial product, process, or service by trade name, trademark, manufacturer, or otherwise, does not necessarily constitute or imply its endorsement, recommendation, or favoring by the United States Government or any agency thereof or its contractors or subcontractors. The views and opinions of authors expressed herein do not necessarily state or reflect those of the United States Government or any agency thereof.

The Role of Cloud Microphysics Parameterization in the Simulation of Mesoscale Convective System Clouds and Precipitation in the Tropical Western Pacific

K. Van Weverberg^{1,2}, A. M. Vogelmann¹, W. Lin¹, E. P. Luke¹, A. Cialella¹, P. Minnis³, M.
Khaiyer⁴, E. R. Boer⁵ and M. P. Jensen¹

¹Brookhaven National Laboratory, Upton, NY, USA

²Georges Lemaître Centre for Earth and Climate Research (TECLIM), Université catholique de
Louvain, Belgium

³National Aeronautics and Space Administration Langley Research Center, Hampton, VA, USA

⁴Science Systems and Applications, Inc., Hampton, VA, USA

⁵Entropy Control, Inc., La Jolla, CA, USA

Abstract

This paper presents a detailed analysis of convection-permitting cloud simulations, aimed at increasing the understanding of the role of parameterized cloud microphysics in the simulation of mesoscale convective systems (MCSs) in the Tropical Western Pacific (TWP). Simulations with three commonly used bulk microphysics parameterizations with varying complexity have been compared against satellite-retrieved cloud properties. An MCS identification and tracking algorithm was applied to the observations and the simulations to evaluate the number, spatial extent, and microphysical properties of individual cloud systems. Different from many previous studies, these individual cloud systems could be tracked over larger distances due to the large TWP domain studied.

The analysis demonstrates that the simulation of MCSs is very sensitive to the parameterization of microphysical processes. The most crucial element was found to be the fall velocity of frozen condensate. Differences in this fall velocity between the experiments were more related to differences in particle number concentrations than to fall speed parameterization. Microphysics schemes that exhibit slow sedimentation rates for ice aloft experience a larger buildup of condensate in the upper troposphere. This leads to more numerous and/ or larger MCSs with larger anvils. Mean surface precipitation was found to be overestimated and insensitive to the microphysical schemes employed in this study. In terms of the investigated properties, the performances of complex two-moment schemes were not superior to the simpler one-moment schemes, since explicit prediction of number concentration does not necessarily improve processes such as ice nucleation, the aggregation of ice crystals into snowflakes, and their sedimentation characteristics.

1. Introduction

High clouds, particularly in the tropics, have been a challenge to climate modeling ever since its inception, even as the microphysical representation of clouds improved and spatial grid spacings became smaller over the years (Randall et al. 2003). One of the main reasons is that our basic understanding of these clouds is still rudimentary at best (Stephens 2005); yet, they are known to be an integral part of the global radiation budget. Hence progress in improving climate simulations depends partly on resolving the microphysical uncertainties surrounding tropical cirrus and convective anvils (Del Genio 2011).

A number of large observational experiments conducted over the past decade (Jensen et al. 2004; Yuter et al. 2005; May et al. 2008, Schmitt and Heymsfield 2009) have unveiled at least some of the factors controlling high tropical clouds. Luo and Rossow (2004) and Mace et al. (2006) demonstrated that about half of the tropical cirrus clouds are detrained from deep convective systems (i.e., are anvil clouds), while the other half are produced in situ, due to gravity waves or large-scale uplift. The predominant source of anvil clouds is detrained ice from convective updrafts, although the long lifetime of tropical cirrus systems suggests that other processes might be involved in replenishing the particles (Ackerman et al. 1988; Luo and Rossow 2004). Anvil clouds can be advected over 1000 km (Luo and Rossow 2004) and extend out more than five times the radius of the main precipitating core (Yuan and Houze 2010). The persistence of high clouds over these large distances from the main updraft cores is highly dependent on (i) the relative humidity of the upper troposphere encompassing convection, and on (ii) the particle sublimation and particle fall speeds (which are both related to their size distributions).

General circulation models (GCMs) are known to have a poor representation of convective updrafts and mass fluxes and, so far, are not capable of explicitly treating precipitating ice species. Grabowski (2000) argues that GCMs also do not fully allow for small-scale and mesoscale processes to feed back to the large scale. Cloud-resolving models (CRMs), however, explicitly resolve convective updrafts and have more advanced cloud microphysics schemes and, thus, are more appropriate to the study of tropical deep convective clouds and their detrainment to anvils. CRMs can also serve as tools for improving GCM parameterizations (e.g. Liang and Wu 2005; Del Genio and Wu 2010) or can be directly used as super-parameterizations within GCMs (e.g. Khairoutdinov and Randall 2001; Benedict and Randall 2009).

Most evaluation studies for tropical convection using CRMs agree that simulated radar reflectivities in the upper troposphere (within the convective cores) are too large, while brightness temperatures are generally too small (Su et al. 1999; Blossey et al. 2007; Zhou et al. 2007; Li et al. 2008; Matsui et al. 2009; Varble et al. 2011). This is often thought to be due to abundant amounts of excessively large frozen condensate at these altitudes. Many of these studies also find an underestimation of the anvil area (or the stratiform precipitation area), which suggests that the frozen condensate is too large, and that it precipitates too effectively (Zhou et al. 2007; Blossey et al. 2007). This is consistent with the findings of recent observational studies (e.g. Heymsfield et al. 2007; Schmitt and Heymsfield 2009) that fall speeds of ice particles at cold temperatures are too fast in the parameterizations used in CRMs.

Increased computing power has allowed CRMs to adopt more complex microphysics schemes over the past decade. Although several approaches that add complexity exist, there is still much debate on the extent to which they also lead to a better representation of cloud systems and which aspects of the microphysics parameterization are most promising for model

improvement. Blossey et al. (2007) found that changes to the effective radii of the precipitation species led to improvements in the fraction of high clouds but, overall, microphysics was found to have little impact. Varble et al. (2011) found a notable impact of microphysics on the hydrometeor distribution, but the more complex models that include more prognostic moments of the size distributions were not superior to the simpler models in terms of cloud-top height and radar reflectivity. Similarly, Wang et al. (2009) found that a more complex microphysics scheme overestimated cirrus clouds during dry periods compared to more simple schemes, while it produced more realistic mixed-phase clouds during convection.

Typically, the aforementioned studies were performed for rather limited domains ($< 500 \text{ km} \times 500 \text{ km}$), while an important fraction of the convection in tropical regions is associated with very large mesoscale convective systems (MCSs) that often exceed such domain sizes. To capture the life cycles of convective systems and understand how these large systems gradually decay into persistent high cirrus clouds, studies with much larger domains are desirable. Further, to understand whether models are capable of simulating key features of organized deep convection, statistics of individual convective systems need to be evaluated. By identifying and tracking these individual cloud systems in model simulations and observations, statistics on their simulated and observed properties can be compared. Finally, many of the aforementioned studies have great value in revealing the systematic model deficiencies that occur in CRMs, but only a few of those studies have been able to pinpoint the reasons for these deficiencies. The authors feel that the latter is essential for making sound recommendations for model improvement.

This study aims to provide further insight into the role of the parameterization of cloud microphysical processes in representing deep convective clouds and their associated anvils. "Anvil" in our study refers to the high cloud that surrounds the core of a deep convective system,

which are defined based on the brightness temperature thresholds suggested by Laing and Fritsch (1993) among others (detailed in section 2.3.2); as such, the anvil region might or might not include regions with stratiform precipitation. Three commonly used microphysics parameterizations with varying complexity have been applied to a week-long simulation of MCSs over the entire Tropical Western Pacific (TWP) domain. An MCS identification and tracking algorithm is applied to satellite-observed and model-simulated top-of-atmosphere (TOA) brightness temperature fields, which enables comparing the MCS statistics among the different schemes under investigation. By examining the differences among these simulations, we were able to discern features in the microphysics parameterization that are critical for proper simulations of convective clouds and their anvils, as well as to determine if and why more complex microphysics schemes yield better simulations of cloud macrophysical structure. Section 2 describes the model setup, experiment design and details of observed and simulated cloud fields. Section 3 discusses the results of the model evaluation and the model sensitivities to microphysics. The main conclusions are given in Section 4.

2. Model description and experiment design

2.1 Model description

The CRM used in this study is the Advanced Research Weather Research and Forecasting model (ARW-WRF) Version 3.3.1 (Skamarock et al. 2007), which is a three-dimensional, fully compressible, nonhydrostatic CRM. The vertical coordinate is a terrain-following hydrostatic

pressure coordinate and the model uses the Runge-Kutta 3rd order integration scheme. The model was integrated for a $30 \times 10^6 \text{ km}^2$ domain, centered on the TWP, applying two-way grid nesting with two nested levels. Data from the National Center for Environmental Prediction (NCEP) Global Forecasting System (GFS; Kalnay et al. 1990) analysis with a 1° horizontal resolution were used as initial conditions and as 6-hourly boundary conditions for the largest domain, that had a 20-km grid spacing and a size of $9,000 \text{ km} \times 6,400 \text{ km}$ (27° N to 27° S and 89° E to 170° E). Within this domain, a 4-km grid spacing domain was nested, covering a $6,900 \text{ km} \times 4,440 \text{ km}$ domain (17° N to 20° S and 100° E to 162° E), which includes most of the TWP. While previous studies often used smaller grid spacings over smaller domains, the grid spacing in this study is constrained by the very large domain size that was used. An overview of the model (and observation) domains is provided in Figure 1. Thirty-five stretched vertical levels were used with a vertical spacing of 60 m near the surface, increasing to 600 m at the 10 km level and 1000 m near the upper-model boundary at 20 km. The model simulations were initialized on 25 December 2003 00 UTC and integrated for a 7 day period ending on 1 January 2004 00 UTC. This period was distinguished by many large MCSs associated with an active Madden-Julian Oscillation (MJO) in the TWP. The first day was considered to be a spin-up period and all analyses in the following sections are for the 6-day period from 26 December 2003 00 UTC to 1 January 2004 00 UTC. The Kain and Fritsch (1993) cumulus parameterization was used in the largest domain, while convection was explicitly simulated in the smaller domain. Shortwave radiation was parameterized following Dudhia (1989) and longwave radiation was parameterized using the Rapid Radiative Transfer Model (RRTM; Mlawer et al. 1997). Three sensitivity experiments were conducted with different microphysics parameterizations, which are further detailed in section 2.2.

2.2 Experiment design

To assess the role of the parameterization of microphysical processes on the development of large convective systems and the related high cloud fields, simulations were performed using three microphysics parameterizations with varying complexity. Roughly in order of increasing complexity, these are the one-moment WRF Single Moment 6-category scheme (Hong and Lim 2006; further referred to as WSM6), the hybrid (two-moment cloud ice and rain) scheme by Thompson et al. (2008; further referred to as THOM), and the full two-moment scheme by Morrison et al. (2009; further referred to as MORR). It should be noted that we implemented an earlier version of MORR than the one currently available in the WRFV3.3.1, due to physically unrealistic model behavior with the latter for these simulations.

Typically, bulk microphysics schemes in CRMs (e.g. Lin et al. 1983 and Rutledge and Hobbs 1984) include 5 hydrometeor types (cloud water, rain, cloud ice, snow and graupel), which are represented by exponential size distributions of which only one moment (usually the third moment) is related to a prognostic variable (usually the mixing ratio):

$$N_x(D) = N_{0x} \exp(-\lambda_x D_x), \quad (1)$$

where N_x is the number of particles per unit volume per unit size range ($\text{m}^{-3} \text{m}^{-1}$), D_x is the maximum dimension of a particle (m), and N_{0x} (m^{-4}) and λ_x (m^{-1}) are the intercept and slope of the exponential size distribution, respectively. The subscript x denotes the hydrometeor type (R , S or G for rain, snow or graupel respectively). Usually, N_{0x} is assumed to be constant, while λ_x is determined by,

$$\lambda_x = \left(\frac{a_{mx} N_{0x} \Gamma(b_{mx} + 1)}{\rho_{air} q_x} \right)^{1/(b_{mx}+1)}, \quad (2)$$

where q_x is the hydrometeor mixing ratio (kg kg^{-1}) and ρ_{air} is the air density (kg m^{-3}). The parameters a_{mx} and b_{mx} are constants for the mass-diameter (m-D) relation $m_x = a_{mx} D_x^{b_{mx}}$, which are provided in Table 1 for the microphysics scheme employed in this study.

While the above approach allows for the hydrometeor size distributions to evolve over time, N_x is constrained only by q_x , which does not allow for observed behaviors such as size sorting or aggregation (Van Weverberg et al. 2012a). To address this limitation, a number of schemes have been developed that include non-constant N_{0x} diagnosed from other prognostic variables such as temperature (Reisner et al. 1998; Hong et al. 2004; Thompson et al. 2004). WSM6, for instance, includes a temperature-dependent N_{0s} , while all other hydrometeors still have constant N_{0x} . THOM is more advanced than WSM6 in that it includes a diagnostic N_{0x} for snow and graupel and explicitly predicts the rain number concentration N_R . Such schemes, in which two prognostic moments of the size distribution are predicted (N_x along with q_x) and prescribing an N_{0x} is no longer necessary, are called two-moment schemes (Ferrier 1994; Seifert and Beheng 2005; Morrison et al. 2009). Many other schemes, such as MORR, are even more advanced, as they predict two moments for all hydrometeors (not just for cloud ice and rain, as in THOM). Note that the MORR scheme used in our simulations is one-moment for cloud water and hence does not predict the N_C . The specific relations used to determine the N_{0x} in all schemes are summarized in Table 1.

The three schemes that we applied also vary considerably in the way that they treat cloud-ice particles and their initiation. While WSM6 only predicts one moment (q_I) of the ice size

distribution (and diagnoses N_I from q_I , following a power law), THOM and MORR explicitly predict two moments of the distribution (q_I and N_I). The number of ice nuclei available for ice initiation is dependent on temperature in all three schemes; WSM6 and MORR allow new crystals to nucleate when supersaturation with respect to ice is achieved at any below-freezing temperature, while THOM also requires that a supersaturation of 20% be reached before nucleation starts.

Apart from differences in the process formulations for the conversions from one hydrometeor into another, further differences between the three schemes include the fall-speed relations used for each species. Some schemes have a fast fallout of hydrometeors, while others have slower sedimentation velocities. Generally, bulk fall speeds of each species are given by:

$$V_x = \frac{a_{vx} \Gamma(b_{mx} + b_{vx} + 1)}{\lambda_x^{b_{vx}} \Gamma(b_{mx} + 1)}, \quad (3)$$

where the parameters a_{vx} and b_{vx} are empirical constants obtained from observed velocity-diameter (V-D) relations. Particles at lower air density experience less drag and fall faster; so within the three schemes, all hydrometeor fall speeds are multiplied by an air density correction factor, which is the square root of the base state air density divided by the model air density. Table 1 provides these constants for each of the microphysics schemes employed here. An overview of the theoretical power-law relations of fall speed versus particle diameter is provided in Figure 2, using the constants a_{vx} and b_{vx} listed in Table 1. All major size distribution characteristics and a number of other key differences between the three schemes are also provided in Table 1.

2.3 Observational data and cloud tracking

2.3.1 Observed and simulated cloud properties

To evaluate the cloud properties in the simulations, we applied the approach of the International Satellite Cloud Climatology Project (ISCCP) to sort clouds into nine classes according to their cloud-top pressure (CTP) and cloud optical thickness (COT) (Rossow and Schiffer 2001). These classes include cirrus (Ci), cirrostratus (Cs), cumulonimbus (Cb), altocumulus (Ac), altostratus (As), nimbostratus (Nb), cumulus (Cu), stratocumulus (Sc) and stratus (St). Thresholds in CTP were used to separate low and middle cloud (680 hPa) and middle and high cloud (440 hPa) in the satellite and the simulations. Thin, intermediately thick, and thick clouds were separated by COT thresholds of 3.6 and 23, respectively.

Hourly satellite data were used from the Geostationary Operational Environmental Satellite (GOES-9) at 4-km resolution, which were sampled to achieve an effective resolution of 8 km. Observed CTP and COT were derived using the Visible Infrared Shortwave-infrared Split-window Technique (VISST), developed at the National Aeronautics and Space Administration (NASA) Langley Research Center (LaRC) and documented in Minnis et al. (2008, 2011). VISST is a four-channel, model-matching method that matches observed radiances to theoretical model calculations for a number of water and ice crystal size distributions. As the visible channel is required to determine COT, only grid cells with a solar zenith angle $< 70^\circ$ have been included in our analysis. Satellite data are available over most of the TWP domain, which covers an area ranging from 10° N to 20° S and 120° E to 180° E. This is slightly more eastward than the model simulation domain (Fig. 1) and in all further satellite-model comparisons we use only the $15 \times$

10^6 km^2 area common between the satellite and the simulations (10° N to 17° S and 120° E to 162° E).

COT in the model simulations is calculated off-line for each hydrometeor separately, following a routine developed by the NASA Goddard Cumulus Ensemble Modeling Group (GCE; Tao et al. 2003). For liquid-water clouds and hail, COT in the visible region is parameterized based on Sui et al. (1998) assuming spherical droplets:

$$\tau_x = 1.5 \times \int \frac{q_x}{R_{ex}} dz, \quad (4)$$

where the subscript x denotes the hydrometeor species (cloud water, rain or graupel) and R_{ex} is its effective radius. Effective radii are derived from the respective microphysical formulations as the ratio of the second to the third moment of the size distributions. For those species represented by a negative exponential size distribution this yields:

$$R_{ex} = \frac{1}{2} \left(\frac{q_x}{a_{mx} N_x} \right)^{1/b_{mx}}, \quad (5)$$

where the constants a_{mx} and b_{mx} are the m-D constants used in equation 2, which are listed in Table 1 for each species and each scheme. For cloud ice and snow, COT is parameterized based on a formula derived for cirrus ice crystals by Fu and Liou (1993):

$$\tau_x = \int 10^4 \times (q_x) \times \left(0.006656 + \frac{3.686 \times 10^{-4}}{R_{ex}} \right) dz, \quad (6)$$

The effective radii are also defined as the ratio of the 2nd to the 3rd moment. Note that THOM assumes a combined exponential and gamma distribution for the snow species and relates the third moment of its distribution to the second moment using empirical relations derived by Field et al. (2005). The relations summarized in their Table 2 are used to determine the second and third moment and hence the snow effective radius for THOM. The empirical coefficients in

equation 6 are obtained from Fu and Liou (1993) by fitting scattering calculations to observed snow size distribution data. Total COT is the sum of all species described by equations 4 and 6.

The use of the above outlined GCE method for the calculation of COT might seem inconsistent with the use of the Dudhia (1989) scheme to calculate the shortwave radiative transfer in the simulations. However, the above method was found to be more consistent with the microphysics parameterizations employed (which is the primary focus of this paper), as the Dudhia (1989) scheme bases its COT calculation on simple empirical relations that, for instance, do not explicitly account for variations in particle effective radii and hence are inconsistent with the size distribution assumptions in the different microphysics schemes. Since our main interest was to understand the role of microphysics on deep convective cloud properties, the COT calculation according to GCE was preferable to the Dudhia (1989) derived COT. (Note that the GCE scheme outlined above is more advanced than the GCE option available in WRF).

Further, given the different methodologies, one cannot guarantee a one-to-one correspondence between the retrieved cloud properties and those computed from the simulations; however, we have used a sophisticated method for computing COT and CTP from the simulations that enables a consistent application to the different microphysics schemes for evaluation against the GOES cloud properties. The comparability of the methods should be adequate for the bulk cloud properties of interest here and, as will be seen, close agreement is often found in the comparisons. Further, Smith et al. (2010) found that GOES-derived properties and CloudSat-derived properties show encouraging correspondence, which provides further confidence in the quality of the observations. Because the satellite cannot discriminate between COT values above 128, all simulated values greater than this value were set to 128.

WRF-simulated CTP is defined as the pressure at the effective emission height of the cloud, which is computed as the level where the integrated longwave absorption COT (from the model top downwards) reaches a value of one (Luo et al. 2010; Van Weverberg et al. 2012b). For consistency with this value, shortwave COT > 2 has been considered in the satellite and model analyses (since shortwave extinction COT is about double the mid-infrared absorption COT). The value of this threshold is somewhat arbitrary, but the same value is applied consistently to the satellite and model fields. A lower value would detect more cloud occurrence in both fields, but retrieved COT at lower values becomes more uncertain because of increased complications presented by the variable land-surface albedo and the increased chance of misinterpreting multi-layered clouds (i.e., thin cirrus overlying low-level cloud). A sensitivity study that uses a shortwave COT threshold of one changes the cloud occurrences but not the overall quality of the model-satellite agreement.

2.3.2 Observed and simulated Mesoscale Convective System identification

In addition to the domain-averaged cloud property statistics, we evaluate how well the structure of convective clouds and their anvils are represented in the various simulations using a cloud-identification and tracking algorithm (Boer and Ramanathan 1997) that was applied to the observations and simulations. This method uses TOA narrowband (11 μm) infrared brightness temperatures (BT). The simulated top-of-model (50 hPa) broadband outgoing longwave radiation (OLR) is translated into TOA narrowband BT using regression coefficients computed off-line using the MODTRAN-v4 multiple-scattering radiative transfer algorithm (Anderson et al. 2001). The computations convert the OLR flux into a narrowband 11- μm flux, translate this flux from

the model top (50 hPa) to the TOA (0 hPa), and then convert the TOA narrowband flux into a radiance from which the equivalent brightness temperature (BT) is determined. After applying a cloudy and clear-sky classification, the algorithm identifies individual cloud systems based on a detection and spread (DAS) cloud identification method (Boer and Ramanathan 1997). In this algorithm, cold cloud regions are first identified ($BT < 240$ K). Next, these clouds are expanded to include the warmer clouds surrounding these cold regions in three steps with consecutively warmer thresholds. Individual clouds are assumed to be distinct systems when their cold BT regions are separated by warmer BT regions. Our primary focus is the detection of MCSs, which are defined following Laing and Fritsch (1993). Each MCS must have a core with a BT less than 219 K and an area larger than $50,000 \text{ km}^2$. Further, each core must be surrounded by an anvil cloud with a BT less than 240 K and with the combined size of the MCS (core and anvil) that exceeds $100,000 \text{ km}^2$. Clouds that are adjacent to an MCS might not be allocated to the MCS if, for instance, they were previously assigned to another cold cloud region that was too small to be classified as an MCS. Also, even though an MCS must contain a total cold area that is large enough, the cold cloud pixels may be contained within multiple small cold areas as long as they are connected via pixels colder than 240 K. The cloud tracker allows for splitting and merging of MCS systems following Williams and Houze (1987). In the following analysis, MCS core regions are defined as the cold part of the MCS ($BT < 219\text{K}$), while anvils are defined as the warmer part of the cloud attached to the MCS ($BT > 219\text{K}$). MCS-tracking has been performed for identical domains in the model and the observations (17° N to 20° S and 100° E to 162° E). However, as observed cloud-property data (COT and CTP) were only available for the slightly eastward domain shown in Figure 1, all statistics in the following sections are for the area

common between the model and the observed cloud properties domains, further referred to as analysis domain (Fig. 1).

3. Results

3.1 ISCCP Cloud Classification

As an example, Figure 3 shows a representative snapshot of the spatial distribution of the different cloud classes according to the ISCCP classification, based on the COT and CTP distributions obtained from the satellite retrievals and from the simulations for the three schemes. Figure 4 provides the 6-day average total area covered by the nine ISCCP cloud classes in the observations and the experiments. More cloud cover statistics are given in Table 2. In the observations, high clouds (mainly consisting of cirrostratus) dominate by covering 35% of the entire analysis domain (Table 2 and Fig. 4). Consistent with previous studies using a one-moment microphysics scheme (Blossey et al. 2007, Zhou et al. 2007), the cirrus and cirrostratus cloud cover in WSM6 is significantly underestimated (Fig. 4 and Table 2). Relatively more low-level optically thick clouds are seen for this simulation, compared to the observations.

Caution should be taken when interpreting the low cloud cover, as the presence of high clouds can hide the low clouds underneath. Indeed, the classification employed here cannot discriminate between multilayer clouds. However, since cloud-top height in the model was determined based on infrared COT, similar to how the satellite determines cloud tops, the model and observations would be affected equally by this limitation. Therefore, this limitation is not expected to influence the model-observation comparison, but it should be understood that this

method will underestimate the occurrence of lower clouds when high clouds are present. Of course, this limitation does not apply to the detection of high clouds, which are of primary interest in this study.

Compared to WSM6, more high cloud is simulated by THOM (consistent with Wang et al. 2009) and MORR. While both schemes have realistic amounts of high cloud cover (bold numbers in Table 2), they tend to produce an abundance of clouds that are optically thick (Fig. 4). Hence, although the high cloud fraction is better simulated compared to WSM6, the cirrostratus cover is underestimated, while the clouds categorized as cumulonimbus are largely overestimated (Fig. 4). The distribution over low, middle and high clouds, as well as the total cloud cover, are simulated better by MORR and THOM, compared to WSM6 (bold numbers in Table 2).

The question arises as to what extent these differences in cloud classes are associated with deep convection by MCSs. Using the MCS identification classification of Boer and Ramanathan (1997), the hatched areas on Figure 4 show the area of each cloud class that is identified as being part of an MCS. About half of the high clouds ($CTP < 440$ hPa) in the observations appear to be associated with an MCS for this 6-day period (hatched area in upper bars in Fig. 4), although the fraction of cirrus clouds associated with an MCS is more modest. From Figure 4, MCS-related cirrus and cirrostratus are significantly underestimated in WSM6, while THOM is able to better capture relatively thin high clouds. MORR overestimates the area covered by MCS cirrus clouds and both THOM and MORR have too many MCS-cumulonimbus clouds (Fig. 4).

3.2 MCS statistics

Using the cloud identification and tracking algorithm described in section 2.3.2, MCSs were identified in the observations and in the three model experiments. Statistics on the MCS properties are provided in Table 3 and visualized in Figure 5. MCS anvils and core regions are defined according to the Laing and Fritsch (1993) definitions based on brightness temperatures, as mentioned in section 2.3.2. Consistent with the analysis in section 3.1, WSM6 underestimates the individual MCS size (Fig. 5 and Table 3) and, further, this scheme only produces about half the amount of observed MCS tracks (Table 3). The significant underestimation of MCS-related clouds in this scheme (Figure 4) is hence due to the MCSs being too small and too few in number. The proportion of core versus anvil is quite well captured by all schemes (Fig. 5). THOM closely captures the number and longevity of observed MCS tracks, but overestimates the MCS sizes (Table 3), which results in approximately the observed total MCS cloud cover (last column in Table 2). MORR simulates too few MCS tracks compared to the observations, but the MCSs are too large and are too long-lived (Table 3), which leads to the MCS cloud cover being significantly overestimated (Table 2). While individual track locations are different for the observations and each of the simulations, tracks more or less equally develop over ocean and land (not shown).

A number of average cloud properties associated with the observed and simulated core and anvil regions of the MCSs are listed in Table 3. All simulations produce anvils that are too optically thick (consistent with Blossey et al. 2007, Li et al. 2008, Varble et al. 2011, Powell et al. 2012) with brightness temperatures that are too low (consistent with e.g. Li et al. 2008, Matsui et al. 2009, Varble et al. 2011). This suggests that the anvils consist of excessive condensate concentrations aloft. It should be mentioned that many of the aforementioned studies also found that the physically thinnest portion of anvil clouds were too optically thin or too

small. Recall, however, that anvils in our simulations are defined differently than in most of these studies and that we do not include anvils with COT thinner than 2 in our analysis, making it hard to compare our results for thin anvil clouds directly to these previous studies. COT is well captured in the core regions, although the BT is 4 to 5 K too warm in all simulations. Table 3 also shows that the observed cloud-top pressure (CTP) in the core region is generally much smaller than for the anvils. All simulations reproduce this difference but, while the (total) CTP for the WSM6 MCS systems is too high (low in altitude), in MORR and THOM CTP is too low (too high in altitude), consistent with e.g. Powell et al. (2012). Of the three simulations, THOM seems to perform best in terms of the MCS cloud properties listed in Table 3.

3.3 MCS dynamics

Microphysics can affect the MCS properties through, for instance, the release of latent heat that modulates the MCS dynamics. To assess whether the larger MCSs in THOM and MORR (discussed above) and the lack of MCS-tracks in WSM6 and MORR are related to such dynamical influences, the average updraft properties for the analysis domain and for the MCS cores are shown in Figure 6 for all experiments. WSM6 has a smaller total updraft mass-flux associated with its MCSs than THOM and MORR (Fig. 6a), but over the analysis domain the total updraft mass-flux in all schemes is very similar (Fig. 6c). Further, the mean updraft speeds are remarkably similar among the three schemes (Fig. 6b and d), although the THOM values in the upper troposphere within MCSs tend to be slightly larger than for the other schemes. This is consistent with Wu et al. (2009), who found updraft strengths to be very similar when THOM or WSM6 was employed during the active monsoon season in the TWP. Figure 7 provides more

details on how the updrafts are organized within each of the simulations. Again, all three schemes seem to behave very similarly. The number of updrafts (Fig. 7b), their individual sizes (Fig. 7c), and their mean updraft speeds (Fig. 6d) are not significantly different between the experiments, which leads to the very similar domain-total updraft mass-fluxes (Fig. 6c). This suggests that differences in the properties and organization of the updrafts do not seem to play an important role in causing the very different MCS properties found between the different schemes. This points to a potentially more important role of the microphysical processes themselves, as is discussed next.

3.4 MCS microphysics

3.4.1 Vertical profiles

Besides its influence on dynamics, the impact of the microphysics scheme on deep convection might be closely related to the microphysical processes. Differences in particle size distributions, for instance, can modulate the particle fall speeds or the rate of processes such as deposition and sublimation. Contoured frequency by altitude diagrams (CFADs; Yuter and Houze 1995) of hydrometeor mixing ratio, number concentration, particle diameter and vertical fall velocities for all precipitating species are provided in Figures 8-11 (cloud water profiles are not shown). The CFADs are calculated for the entire domain and simulation period.

The three microphysics schemes produce very different vertical profiles of q_l (Fig. 8a to c). Cloud ice is most abundant throughout the troposphere in WSM6 (Fig. 8a), although the mixing ratios do not reach very large values. Cloud ice is somewhat less abundant in MORR (Fig. 8b)

but reaches larger mixing ratios in the upper troposphere, while THOM (Fig. 8c) produces the least cloud ice, consistent with e.g. Wang et al. (2009). Also remarkable are the large mean cloud-ice diameters (Fig. 9a and b) and fall speeds (Fig. 11a and b) throughout the atmosphere in WSM6 and at mid-levels (5 to 10 km) in MORR, which are much larger than usually observed for cloud ice particles (e.g. Lawson et al. 2006, Heymsfield et al. 2007). MORR and THOM both include a size threshold for cloud ice; the portion of the cloud-ice size distribution that is larger than this threshold is automatically transferred to the snow species. In THOM, this size threshold is 5 times smaller compared to MORR (volume-weighted mean diameter of about 1×10^{-4} m versus about 5×10^{-4} m), which rapidly transfers large ice particles into the snow species. As THOM also requires air to be supersaturated by 20% for nucleation to take place, q_I is smaller in THOM than in the other schemes.

Near the tropopause at 16 km, the bulk of the ice particles in MORR are much smaller than below (Fig. 9b) and become comparable to the sizes of ice particles in THOM (Fig. 9c). WSM6 has rather large D_I and hence V_I even at this altitude (Fig. 9a and 11a). Recall that WSM6 is the only scheme that does not explicitly predict N_I (Table 1), but diagnoses N_I from q_I . This is unlike many other one-moment microphysics schemes that diagnose N_I from temperature (e.g. Lin et al. 1983, Rutledge and Hobbs 1984). Apparently, the relation used in WSM6 produces very small N_I aloft (Fig. 10a vs. b and c) and hence very large particles that fall out more quickly compared to THOM and the upper levels in MORR (Fig 11a to c). N_I in MORR and THOM is explicitly predicted and nucleation of new ice crystals is a function of air density and temperature, leading to more numerous particles near the tropopause (Fig. 10b and c). THOM limits the maximum number of crystals to $2.5 \times 10^5 \text{ m}^{-3}$ while MORR allows the maximum ice number concentration to reach $1 \times 10^7 \text{ m}^{-3}$, which results in the MORR N_I being even larger than for THOM.

Greater similarities exist between the microphysics schemes for the snow species (Fig. 8d to f). The vertical profiles of q_S (Fig. 8) above the melting layer (about 5 km) are dominated by snow in all three schemes. Snow content is somewhat lower in WSM6, due to the absence of the size threshold for cloud ice as discussed above. THOM has much more snow in the upper troposphere (Fig. 8f), which is related to the large N_S (Fig. 10f) and smaller fall velocities (Fig. 11f) at these altitudes. As the snowflakes are much more numerous in THOM in the upper troposphere, compared to WSM6 and MORR (Fig. 10d to f), snow depositional growth and competition for water vapor at these altitudes will be much larger. Therefore, the q_I near the tropopause cannot grow as large in THOM as in WSM6 and MORR. Only when the snowflakes in THOM become less numerous below 10 km can q_I grow larger through depositional growth, leading to the spike in the q_I profile in THOM near this level (Fig. 8c).

For graupel, the q_G , D_G and V_G between WSM6 and MORR are similar (Fig. 8, 9 and 11g and h). THOM, however, produces smaller q_G (Fig. 8i), consistent with findings by Wang et al. (2009).

3.4.2 Implications for MCS properties

The main feature emerging from the analysis of the vertical hydrometeor profiles in the previous section is that WSM6 seems to be dominated by faster falling hydrometeor species compared to MORR and THOM, mainly in the upper troposphere. Although cloud ice is abundant in this scheme, this ice falls out nearly as quickly as the snow species, even near the tropopause (Fig. 10a and d). MORR, on the other hand, has the most abundant cloud ice near the tropopause, which falls very slowly (Fig 10b). At lower altitudes, below 13 km, the ice diameter

(Fig. 10b) and fall speed (Fig 11b) rapidly increase and MORR becomes dominated by fast falling species. Very slow fallout of hydrometeors near the tropopause also occurs in THOM. While cloud ice is rare in this scheme throughout the atmosphere, THOM is dominated by remarkably slow snow fallout above 10 km compared to the other schemes. The slow fallout of snow in the upper troposphere is further demonstrated by Figure 12, which relates q_s to the fall speed for each of the schemes for altitudes above 10 km. From this figure, snow falls about half as fast in THOM compared to the other schemes for any q_s . Recall from Figure 2 that this is not due to differences in the fall speed-diameter power-law relation applied in THOM; so the difference must be attributed to THOM having larger N_s of smaller snowflakes compared to the other two schemes (Fig. 9f and 10f).

While MORR explicitly predicts N_s , it has to be diagnosed in one-moment treatments in WSM6 and THOM. WSM6 represents the snow size distribution by an exponential function; N_s can be diagnosed from λ_s and N_{0s} following:

$$N_s = \frac{N_{0s}}{\lambda_s}, \quad (7)$$

where N_{0s} is provided in Table 1 and λ_s is given by equation 2. THOM, however, has a combined exponential and gamma snow size distribution (Table 1) and, hence, diagnoses N_s from empirical relations derived by Field et al. (2005) as follows:

$$N_s = a(T_c) \times \left(\frac{\rho q_s}{a_{ms}} \right)^{b(T_c)}, \quad (8)$$

where the coefficient $a(T_c)$ and exponent $b(T_c)$ are polynomial functions of temperature T_c (given in Table 2 in Field et al. 2005) and a_{ms} is provided in Table 1. The relations by Field et al. (2005) were derived for mid-latitude stratiform clouds with temperatures ranging from -55°C to

0°C. When applied at the very low temperatures ($< -80^{\circ}\text{C}$) near the tropical tropopause this yields N_S that are a couple orders of magnitude larger than for the other schemes. Since the snow diameter, D_S , is dependent on N_S , this also yields smaller snow particles (Fig. 9f) that will fall much more slowly (Fig. 2 and 11f).

Figure 13 shows vertical cross sections through the MCSs, depicted in Figure 3, and provides further insight into the simulated MCS structure. The left hand panels represent the dynamic features of the average MCSs, showing the in- and outflow strength (colors and arrows), as well as the vertical velocities of snow (solid contours) and cloud ice (dashed contours). Again, this figure features the very small sedimentation velocities of snow aloft in THOM (Fig. 13e) compared to the other schemes (Fig. 13a and c). Obviously, this leads to a larger buildup of condensate and this condensate (mainly snow) has nowhere to go but be lofted to the tropopause outflow of the MCS. The cloud shield in MORR (Fig. 13d) is about as extensive as in THOM (Fig. 13f), but it consists mainly of slowly falling ice crystals, as denoted on the left hand panels in Figure 13 and the CFADs in Figure 8-11. Also note that the upper level outflow strengths are quite similar between the three schemes. From the right hand panels in Figure 13, it is clear that clouds spread out against the tropopause much farther in THOM and MORR compared to WSM6. Snow is hence transported over large distances from the main updraft cores in THOM, while the same is true for cloud ice in the MORR scheme.

From the above analysis, the reason for the larger MCS systems in MORR and THOM, compared to WSM6, resides in the presence of slowly falling hydrometeor species near the tropopause. These hydrometeors spread horizontally in the divergent upper levels around the MCS cores more rapidly than they sediment to lower altitudes. This produces a larger buildup of

condensate in the upper troposphere in both schemes – albeit for different reasons – compared to WSM6.

To provide further support for the hypothesis that slower snow fall speeds aloft could invoke larger MCS systems, an additional sensitivity experiment was conducted. This experiment, referred to as MORR_SS, had an identical setup as the MORR experiment, except that the air density correction for the snow species was omitted. In this way, the effect of reduced snow fall speeds with higher altitude in the THOM scheme could be mimicked. The relation between q_s and V_s in MORR_SS is shown in Figure 12c. Above 10 km AGL, snow fall speeds approached those of the THOM scheme closely in this experiment. The statistics of MCS properties in this scheme are provided in Table 3. The average size of the MCSs grew by nearly 40% in MORR_SS compared to MORR and the number of tracks increased, consistent with the explanation that the slow snow fallout aloft is responsible for the large MCSs in THOM.

3.4.3 Implications for MCS upper tropospheric humidity levels

From Figure 13b, d and f, the larger upper tropospheric cloud extent in MORR and THOM is associated with moister upper levels compared to WSM6. Figure 14 shows the vertical profile of divergence associated with mid-level updrafts. From this figure and from the left hand panels in Figure 13, the upper level outflow characteristics in all schemes are very similar. Hence, this enhanced upper-level moisture in THOM and MORR must originate from the sublimation of snow and cloud ice, which returns significant portions of the condensate back to the vapor phase. Indeed, from the formulation of the depositional growth rate parameterization, the slower the ice

particles fall and the more numerous they are, the more sublimation that will take place in an unsaturated environment. A debate is ongoing concerning whether the often observed elevated-moisture plume downwind from MCSs is mainly attributable to the sublimation of ice, or to vapor advection from the updraft core regions (Soden 2004, Luo and Rossow 2004, Wright et al. 2009). Our analysis shows that – at least within this CRM – vapor is most likely originating from sublimation of ice, consistent with Wright et al. (2009). While all schemes have similar upper-air outflow dynamics, the schemes that produce the slowest ice/snow sedimentation and largest ice/snow mass and number concentration aloft (and hence the most sublimation) eventually produce a moister upper troposphere.

3.5 MCS surface precipitation

The above-described influence of microphysics parameterization on the formation of clouds may impact the fallout of condensate at lower levels and surface precipitation. Figure 15 and Table 4 summarize the main features of simulated and observed accumulated surface precipitation. Given the different behaviors of the three schemes in terms of cloud properties, it is remarkable that domain average surface precipitation among the schemes is so similar. Since the updraft properties among the schemes are very similar as well (section 3.2.2), this indicates that the precipitation efficiencies within the three schemes are more or less identical. However, total cloudiness and hence the amount of water stored aloft is larger in MORR and THOM, compared to WSM6. Moreover (and probably more importantly), much of the upper level cloud in MORR and THOM sublimates to the vapor phase (e.g. Figure 13). Since the total ice and snow content in THOM is about three times larger than in WSM6, the additional sublimation in

THOM will not be negligible (a more detailed study of the magnitude of the microphysics conversion processes would be required to provide a more precise quantitative assessment of the impact of sublimation differences on precipitation efficiencies). Hence, in order to obtain similar precipitation efficiencies among the three schemes, there must be additional loss of condensed water in WSM6 to match the water losses aloft in the other two schemes.

The precipitation efficiency in CRMs can be very sensitive to rain evaporation rates (e.g. Morrison and Milbrandt 2011), which are largely controlled by the rain drop size (Van Weverberg et al. 2012a). The rain size distribution characteristics for all simulations are provided in Figures 8 to 11 in bottom panels j to l. Further, average vertical profiles of raindrop characteristics for areas with significant surface precipitation are provided in Figure 16a and c. While the q_R (Fig. 8j to l, Fig. 16a) is largest in WSM6 and smallest in THOM, the bulk of the mean rain drop sizes (D_R) in WSM6 are weighted towards small drops (Fig. 9j to l, Fig. 16c) that fall much slower (Fig. 11j to l). Recall that WSM6 is the only scheme that does not explicitly predict the raindrop number concentration but, instead, fixes the rain intercept parameter. The same quantity of rain water, but distributed over smaller drops, has a much larger effective surface area; so, it is likely that more raindrop evaporation takes place in WSM6, reducing its precipitation efficiency compared to those in MORR and THOM. Due to more intense rain evaporation, this is also manifested as a higher relative humidity associated with rainy areas in WSM6's the lower troposphere, compared to the other schemes (Fig. 16e). A more detailed study would be required to provide more evidence for this hypothesis. It should also be noted that MCSs are smaller in WSM6 than in MORR and THOM (section 3.2) and hence a larger portion of the surface precipitation in WSM6 originates from non-MCS related convection (80% versus 50% in MORR and THOM). The proportion of MCS-related surface precipitation

originating from the core versus the anvil area is very similar among the different schemes (not shown).

In terms of surface precipitation, a more striking difference occurs in the peak precipitation rates. Table 4 (5th column) provides the time-averaged domain peak instantaneous surface rain rate (one peak rate for the entire domain per output time). The peak precipitation rate in MORR is considerably lower compared to the other two schemes. Van Weverberg et al. (2012a) suggested that the difference in peak precipitation between the two two-moment microphysics schemes studied could be entirely attributed to differences in the raindrop breakup parameterization. Larger rain drops will be less prone to evaporation and will fall out quicker, which increases the peak precipitation rates. Figures 16b and d provide the raindrop characteristics in all simulations, which are only associated with the most intense precipitation rates ($> 50 \text{ mm hr}^{-1}$). While the mixing ratios among the schemes are rather similar (Fig. 16b), MORR has the smallest drops associated with intense precipitation (Fig. 16d). One of the reasons for this resides in the more active rain drop breakup in the MORR scheme compared to THOM. Drop breakup starts in MORR when they reach a volume-weighted mean diameter of about $0.5 \times 10^{-3} \text{ m}$, while drop breakup starts in THOM only when their mean diameter grows larger than about $0.9 \times 10^{-3} \text{ m}$. More important, however, is the different size limit that both schemes impose on the rain drop diameter. MORR constrains the volume-weighted mean rain drop diameter to about $0.9 \times 10^{-3} \text{ m}$, while the size limit amounts to about $1.2 \times 10^{-3} \text{ m}$ in THOM, which is reflected in the truncation of the CFADs near these size thresholds on Fig. 9k and l. The fixed intercept approach in WSM6 leads to drop sizes that are nearly as large as in THOM within the intense precipitation areas (Fig. 16d), which leads to similar evaporation and fallout and hence peak precipitation rates (Table 4).

An estimate of the observed surface precipitation accumulation for the model domain and simulation period was obtained from the Global Precipitation Climatology Project (GPCP; Adler et al. 2003), established by the World Climate Research Program. GPCP provides daily global surface precipitation data at 1° resolution. To obtain an estimate of the uncertainty associated with the observed surface precipitation, the Tropical Rainfall Measuring Mission (TRMM; Kummerow et al. 1998, 2000) daily precipitation accumulations are also provided, which are available with daily temporal resolution at 0.25° resolution. Table 4 shows precipitation characteristics for both datasets, aggregated to GPCP's 1° resolution. From this table, the domain-average precipitation accumulations are quite similar between GPCP and TRMM, but the maximum accumulations are somewhat larger in TRMM. Figure 15 and Table 4 show that all simulations significantly overestimate the domain-average precipitation accumulations by 30-40%, even when considering the relative negative bias error of about 10 to 15% in GPCP in the TWP (Adler et al. 2012). The location of the intense precipitation corridor north of Papua New Guinea is reasonably well captured, while a dry bias exists in all simulations across northern Australia. In part, this could be associated with a wet bias in the GPCP observed precipitation in northern Australia that occurs in southern hemispheric summer (Adler et al. 2012).

Reasons for the general overestimation of surface precipitation might not entirely be associated with the microphysics parameterization. Recall that the grid spacing used in our simulation might still be too coarse to fully resolve convective updrafts. Indeed, observational studies of convective updrafts over tropical oceans (Lucas et al. 1994, Anderson et al. 2005, Heymsfield et al. 2010) typically report updraft diameters that are smaller than 4 km. Updrafts in our simulations were generally much wider than observed (Fig. 7a), consistent with Deng and Stauffer (2006), that likely results in too much upward mass transport. Also, Bryan and Morrison

(2012) report that detrainment of clouds is very dependent on the model resolution. They found surface precipitation to be up to 30% lower when using a 250 m grid spacing compared to simulations using a 4-km grid spacing, due to the larger detrainment rates. Varble et al. (2011) found smaller (but still important) surface precipitation overestimations over the TWP, mainly in the convective regions, using a suite of CRMs with higher resolution (about 1 km grid spacing). Too much upward mass transport and a lack of detrainment in our simulations might play an important role in the overestimated surface precipitation and optical thickness.

4. Summary and discussion

Progress in the representation of convection-associated cloud structures within cloud-resolving models can only be achieved if the physical reasons for discrepancies between the different models are truly understood. This paper presents a detailed analysis of convection-permitting simulations that is aimed at increasing the understanding of the role of parameterized cloud microphysics in the simulation of MCSs in the Tropical Western Pacific. Simulations with three commonly used bulk microphysics parameterizations with varying complexity have been evaluated against satellite-retrieved cloud properties. An MCS identification algorithm was applied to the observations and the simulations to evaluate the properties of individual cloud systems. Different from many previous studies, these individual cloud systems could be tracked over large distances due to the large domain employed.

The analysis demonstrates that the simulation of MCSs is very sensitive to the parameterization of microphysical processes. The most crucial element was found to be the fall

velocity of frozen condensate in the upper troposphere, which supports earlier analysis performed with GCMs (e.g. Sanderson et al. 2008). In our study, microphysics schemes that have slow sedimentation rates of ice aloft experience a larger buildup of condensate. This condensate is picked up by the updraft outflow near the tropopause and only gradually sublimates; so, anvils in these systems extend much farther from the updraft cores compared to schemes that experience faster fallout of ice. The two schemes with the slowest fallout of ice particles near the tropopause (MORR and THOM) produce larger MCS systems than observed, while the scheme with faster fallout (WSM6) simulates smaller MCSs than observed. Although MORR and THOM both produce large MCS systems, MORR does so because of abundant slowly falling cloud ice particles; THOM does so because of the very small and slowly falling snowflakes aloft, while cloud ice is scarce in this scheme. This adds to the discussion on the definition of the different hydrometeor types in bulk microphysics schemes. Indeed, the tiny snowflakes aloft in THOM resemble cloud ice particles, while the large cloud ice particles in WSM6 and at lower altitudes in MORR have fall speeds and diameters that approach those of snow. It seems to be crucial to limit cloud ice to small particle sizes (and hence slow fall speeds), while still maintaining sufficient mass of small particles aloft (e.g. by not converting it too readily to the faster falling snow). Of all simulations, THOM produced the most realistic MCS cloud properties; although all simulations produced anvils that were too thick and had brightness temperatures that were too cold. Elevated levels of relative humidity in the upper troposphere, downwind from MCSs, seemed to predominantly originate from ice sublimation rather than from vapor advection, supporting the findings by Wright et al. (2009).

Despite the larger cloudiness in MORR and THOM compared to WSM6, the precipitation efficiencies in all schemes were very similar, as updraft properties and surface precipitation

accumulation hardly differed. This could be because more intense evaporation of raindrops in WSM6 compensates for the smaller cloudiness and hence sublimation of ice aloft, compared to the other two schemes. However, this needs further investigation. All simulations significantly overestimated surface precipitation. Along with overestimated convective cloud optical thickness, this suggests that updraft mass fluxes in all simulations were too large. Some studies suggest that, for the 4-km spatial resolution employed here, updrafts are forced on larger-than-natural scales (Deng and Stauffer 2006) and clouds experience a lack of detrainment (Bryan and Morrison 2012), which might explain at least part of the overestimated surface precipitation. Observations of updraft mass fluxes from radar would be helpful to improve our understanding of the impact that horizontal grid spacing has on updraft properties. Also, the conjecture that updraft mass fluxes are too large raises the question as to whether the excessive MCS sizes in the MORR and THOM experiments reflect an inherent deficiency in the model updraft dynamics, with the microphysics being better represented than the simulations suggest. Further research is needed to separate dynamical deficiencies from the representation of microphysics.

In our simulations, the more complex two-moment schemes did not perform better than the simpler one-moment schemes. The slower fall velocities in THOM's one-moment snow treatment, which had more realistic anvils and the correct number of MCSs, were found to be due to the large number concentration aloft of snowflakes (rather than from different velocity-diameter relations). Hence, to better capture the representation of high tropical clouds, more attention should be given to the processes that influence snow and ice number concentrations, such as nucleation of ice crystals and the subsequent aggregation into larger snowflakes. Although high-quality observations of microphysical properties have become available over recent years (e.g. Frey et al 2011, Protat et al. 2007, Delanoe et al. 2005), many more

observations (mainly of ice particle size distributions) of tropical anvil clouds are sorely needed to develop improved parameterizations.

It should be stressed that this study focused on clouds associated with MCSs and did not look into non-convective high clouds or very thin anvil clouds ($\text{COT} < 2$). The non-convective high cloud cover was underestimated in all simulations (Fig. 4, non-hatched areas) and was rather insensitive to microphysics. Further, our study focused on the impact of microphysics on convective clouds and did not study any radiative feedbacks associated with these clouds. Such feedbacks have been shown to play a significant role in radiative heating of anvil and cirrus clouds (McFarlane et al. 2007, Powell et al. 2012), but usually they play a secondary role on the short time-scales used in our study (e.g. Wang et al. 2009). However, given the very different cloud and hydrometeor properties among the schemes in our study, differences in radiative fluxes are probably large as well and should certainly not be ignored on longer time scales. In order to study such radiative feedback, a better coupling of the parameterization of microphysical processes and radiative processes is essential.

5. Acknowledgements

Research by Van Weverberg, Vogelmann, Lin, Luke, Cialella and Jensen was supported by the Laboratory Directed Research and Development Program at Brookhaven National Laboratory, the U.S. Department of Energy's Atmospheric Science Program Atmospheric System Research (ASR), an Office of Science Office of Biological and Environmental Research program, under contract DE-AC02-98CH10886, and by the Earth System Modeling Program via the FASTER project (www.bnl.gov/esm). M. Khaiyer and P. Minnis were also supported by the

ASR under Inter agency Agreement, DE-SC0000991/003. We kindly acknowledge the use of the NY Blue, a Blue Gene/L supercomputer that was used for the WRF simulations. We thank three anonymous reviewers for their suggestions that led to major improvements to the paper.

6. References

- Ackerman, T. P., K. N. Liou, F. P. J. Valero, and L. Pfister, 1988: Heating rates in tropical anvils. *J. Atmos. Sci.*, **45**, 1606-1623.
- Adler, R.F., G.J. Huffman, A. Chang, R. Ferraro, P.-P. Xie, J. Janowiak, B. Rudolf, U. Schneider, S. Curtis, D. Bolvin, A. Gruber, J. Susskind, P. Arkin, E. Nelkin, 2003: The Version-2 Global Precipitation Climatology Project (GPCP) monthly precipitation analysis (1979-present). *J. Hydrometeor.*, **64**, 1147-1167.
- , G. Gu, G.J. Huffman, 2012: Estimating climatological bias errors for the Global Precipitation Climatology Project (GPCP). *J. Appl. Meteor.*, **51**, 84-99.
- Anderson, N.F., C.A. Grainger, J.L. Stith, 2005: Characteristics of strong updrafts in precipitation systems over the central tropical Pacific Ocean and in the Amazon. *J. Appl. Meteor.*, **44**, 731-738.
- Anderson, G. P., A. Berk, P. K. Acharya, M. W. Matthew, L. S. Bernstein, J. H. Chetwynd, H. Dothe, S. M. Adler-Golden, A. J. Ratkowski, G. W. Felde, J. A. Gardner, M. L. Hoke, S. C. Richtsmeier, and L. S. Jeong, 2001: MODTRAN4, version 2: Radiative transfer modeling. *SPIE-Int. Soc. Opt. Eng.*, **4381**, 455– 459.
- Benedict, J.J., D.A. Randall, 2009: Structure of the Madden-Julian Oscillation in the superparameterized CAM. *J. Atmos. Sci.*, **66**, 3277-3296.
- Blossey, P.N., C.S. Bretherton, J. Cetrone, M. Kharoutdinov, 2007: Cloud-resolving model simulations of KWAJEX: Model sensitivities and comparisons with satellite and radar observations. *J. Atmos. Sci.*, **64**, 1488-1508.

- Boer, E.R., V. Ramanathan, 1997: Lagrangian approach for deriving cloud characteristics from satellite observations and its implications to cloud parameterization. *J. Geophys. Res.*, **102**, 21383-21399.
- Bryan, G.H., H. Morrison, 2012: Sensitivity of a simulated squall line to horizontal resolution and parameterization of microphysics. *Mon. Wea. Rev.*, **140**, 202-225.
- Cox, G.P., 1988: Modelling precipitation in frontal rainbands. *Quart. J. Roy. Meteor. Soc.*, **114**, 115-127.
- Delanoe, J., A. Protat, J. Testud, D. Bouniol, A. Heymsfield, A. Bansemer, P. R. A. Brown, and R. M. Forbes, 2005: Statistical properties of the normalized ice particle size distribution. *J. Geophys. Res.*, **110**, D10201, doi:10.1029/2004JD005405.
- Del Genio, A. D., and J. Wu, 2010: The Role of Entrainment in the Diurnal Cycle of Continental Convection. *J. Climate*, **23**, 2722–2738.
- , 2011: Representing the sensitivity of convective cloud systems to tropospheric humidity in general circulation models. *Surv. Geophys.*, doi: 10.1007/s10712-0119148-9
- Deng, A., Stauffer, D. R., 2006: On improving 4-km mesoscale model simulations. *J. Appl. Meteorol. and Climatology*, **45**, 361-381.
- Dudhia, J., 1989: Numerical study of convection observed during the winter monsoon experiment using a mesoscale two-dimensional model. *J. Atmos. Sci.*, **46**, 3077-3107.
- Ferrier, B. S., 1994: A double-moment multiple-phase four-class bulk ice scheme, Part I: description. *J. Atmos. Sci.*, **51**, 249-280.

- , W.-K. Tao, J. Simpson, 1995: A double-moment multiple-phase four-class bulk ice scheme. Part II: Simulations of convective storms in different large-scale environments and comparison with other bulk parameterizations. *J. Atmos. Sci.*, **52**, 1001-1033.
- Field, P. R., R. J. Hogan, P. R. A. Brown, A. J. Illingworth, T. W. Choularton, R. J. Cotton, 2005: Parameterization of ice-particle size distributions for mid-latitude stratiform cloud. *Quart. J. Roy. Meteor. Soc.*, **131**, 1997-2017.
- Frey, W., S. Borrmann, D. Kunkel, R. Weigel, M. de Reus, H. Schlager, A. Roiger, C. Voigt, P. Hoor, J. Curtius, M. Krämer, C. Schiller, C. M. Volk, C. D. Homan, F. Fierli, G. Di Donfrancesco, A. Ulanovsky, F. Ravegnani, N. M. Sitnikov, S. Viciani, F. D'Amato, G. N. Shur, G. V. Belyaev, K. S. Law, and F. Cairo, 2011: In situ measurements of tropical cloud properties in the West African monsoon: upper tropospheric ice clouds, mesoscale convective system outflow, and subvisual cirrus. *Atmos. Chem. Phys.*, **11**, 5569-5590.
- Fu, Q., K.-N. Liou, 1993: Parameterization of the radiative properties of cirrus clouds. *J. Atmos. Sci.*, **50**, 2008-2025.
- Grabowski, W.W., 2000: Cloud microphysics and the tropical climate: Cloud-resolving model perspective. *J. Climate*, **13**, 2306-2322.
- Heymsfield, A. J., M. Kajikawa, 1987: An improved approach to calculating terminal velocities of plate-like crystals and graupel. *J. Atmos. Sci.*, **44**, 1088-1099.
- , L.J. Donner, 1990: A scheme for parameterizing ice-cloud water content in general circulation models. *J. Atmos. Sci.*, **47**, 1865-1877.
- , G.-J. van Zadelhoff, D.P. Donovan, F. Fabry, R.J. Hogan, A.J. Illingworth, 2007: Refinements to ice particle mass dimensional and terminal velocity relationships for ice

- clouds. Part II: Evaluation and parameterizations of ensemble ice particle sedimentation velocities. *J. Atmos. Sci.*, **64**, 1068-1088.
- Heymsfield, G.M., L. Tian, A.J. Heymsfield, L. Li, S. Guimond, 2010: Characteristics of deep tropical and subtropical convection from nadir-viewing high-altitude airborne Doppler radar. *J. Atmos. Sci.*, **67**, 285-308.
- Hong, S.-Y., J. Dudhia, S.-H. Chen, 2004: A revised approach to ice microphysical processes for the bulk parameterization of clouds and precipitation. *Mon. Wea. Rev.*, **132**, 103-120.
- , J.-O. Jade Lim, 2006: The WRF single-moment 6-class microphysics scheme (WSM6). *J. Korean Meteor. Soc.*, **42**, 129-151.
- Houze, R.A., P.V. Hobbs, P.H. Herzegh, D.B. Parsons, 1979: Size distributions of precipitation particles in frontal clouds. *J. Atmos. Sci.*, **36**, 156-162.
- Jensen, E.J., D. Starr, O. Toon, 2004: Mission investigates tropical cirrus clouds. *Eos*, 85, 45-50.
- Kain, J. S., J. M. Fritsch, 1993: Convective parameterization for mesoscale models: The Kain-Fritsch scheme. The Representation of Cumulus Convection in Numerical Models. *Meteorol. Monogr.*, **24**, 165-170.
- Kalnay, E., M. Kanamitsu, W.E. Baker, 1990: Global numerical weather prediction at the National-Meteorological Center. *Bull. Amer. Meteor. Soc.*, **71**, 1410-1428.
- Khairoutdinov, M. F., and D.A. Randall, 2001: A cloud resolving model as a cloud parameterization in the NCAR Community Climate System Model: Preliminary Results. *Geophys. Res. Lett.*, **28**, 3617-3620
- Kummerow, C., W. Barnes, T. Kozu, J. Shiue, J. Simpson, 1998: The tropical rainfall measuring mission (TRMM) sensor package. *J. Atmos. Oceanic. Technol.*, **15**, 809-817.

- , J. Simpson, O. Thiele, W. Barnes, A.T.C. Chang, E. Stocker, R.F. Adler, A. Hou, E. Wentz, P. Ashcroft, T. Kozu, Y. Hong, K.Okamoto, I. Iguchi, H. Kuroiwa, E. Im, Z. Haddad, G. Huffman, B. Ferrier, W.S. Olson, E. Zipseri, E.A. Smith, I.I. Wilheit, G. North, T. Krishnamurti, K. Nakamura, 2000: The status of the tropical rainfall measuring mission (TRMM) after two years of orbit. *J. Appl. Meteor.*, **39**, 1965-1982.
- Laing, A.G., J.M. Fritsch, 1993: Mesoscale convective systems over the Indian monsoon region. *J. Climate*, **6**, 911-919.
- Lawson, R.P., B. Baker, B. Pilson, Q. Mo, 2006: In situ observations of the microphysical properties of wave, cirrus and anvil clouds. Part II: Cirrus clouds. *J. Atmos. Sci.*, **63**, 3186-3203.
- Li, Y., E.J. Zipser, S.K. Krueger, M. A. Zulauf, 2008: Cloud-resolving modelling of deep convection during KWAJEX. Part I: Comparison to TRMM satellite and ground-based radar observations. *Mon. Wea. Rev.*, **136**, 2699-2712.
- Liang, X.Z., X.Q. Wu, 2005: Evaluation of a GCM subgrid cloud-radiation interaction using cloud-resolving model simulations. *Geophys. Res. Lett.*, **32**, doi: 10.1029/2004GL022301
- Lin, Y.- L., Farley, R. D., H. D. Orville, 1983: Bulk parameterization of the snow field in a cloud model. *J. Clim. Appl. Meteorol.*, **22**, 1065-1092.
- Liu, J. Y., H. D. Orville, 1969: Numerical modeling of precipitation and cloud shadow effects on mountain-induced cumuli. *J. Atmos. Sci.*, **26**, 1283-1298.
- Locatelli, J. D., P. V. Hobbs, 1974: Fall speeds and masses of solid precipitation particles. *J. Geophys. Res.*, **79**, 2185-2197.
- Lucas, C., E.J. Zipser, M.A. Lemone, 1994: Vertical velocity in oceanic convection off tropical Australia. *J. Atmos. Sci.*, **51**, 3183-3193.

- Luo, Z., W.B. Rossow, 2004: Characterizing tropical cirrus life cycle, evolution, and interaction with upper-tropospheric water vapour using lagrangian trajectory analysis of satellite observations. *J. Climate*, **17**, 4541-4563.
- Luo, Z. J., G. Y. Liu, and G. L. Stephens. 2010: Use of A-Train data to estimate convective buoyancy and entrainment rate. *Geophys. Res. Lett.*, **37**, L09804, doi:10.1029/2010GL042904.
- Mace, G.G., M. Deng, B. Soden, E. Zipser, 2006: Association of tropical cirrus in the 10-15 km layer with deep convective sources: An observational study combining millimeter radar data and satellite-derived trajectories. *J. Atmos. Sci.*, **63**, 480-503.
- Matsui, T., X. Zeng, W.- K. Tao, H. Masunaga, W. S. Olson, S. Lang, 2009: Evaluation of long-term cloud-resolving model simulations using satellite radiance observations and multifrequency satellite simulators. *J. Atmos. Ocean. Tech.*, **26**, 1261-1274.
- May, P.T., J.H. Mather, G. Vaughan, C. Jakob, G.M. McFarquhar, K.N. Bowen, G.G. Mace, 2008: The tropical warm pool international cloud experiment. *Bull. Amer. Meteor. Soc.*, **89**, 629-645.
- McFarlane, S. A., J. H. Mather, and T. P. Ackerman, 2007: Analysis of tropical radiative heating profiles: A comparison of models and observations. *J. Geophys. Res.*, **112**, doi:10.1029/2006JD008290.
- Minnis, P., L. Nguyen, R. Palikonda, P. W. Heck, D. A. Spangenberg, D. R. Doelling, J. K. Ayers, W. L. Smith, Jr., M. M. Khaiyer, Q. Z. Trepte, L. A. Avey, F.-L. Chang, C. R. Yost, T. L. Chee, and S. Sun-Mack, 2008: Near-real time cloud retrievals from operational and research meteorological satellites. *Proc. SPIE Europe Remote Sens. 2008, Cardiff, Wales, UK*, 15-18 September, **7107-2**, 8 pp.

- , S. Sun-Mack, D. F. Young, P. W. Heck, D. P. Garber, Y. Chen, D. A. Spangenberg, R. F. Arduini, Q. Z. Trepte, W. L. Smith, Jr., J. K. Ayers, S. C. Gibson, W. F. Miller, V. Chakrapani, Y. Takano, K.-N. Liou, Y. Xie, and P. Yang, 2011: CERES Edition-2 cloud property retrievals using TRMM VIRS and Terra and Aqua MODIS data, Part I: Algorithms. *IEEE Trans. Geosci. Remote Sens.*, **49**, 11, 4374-4400.
- Mlawer, E.J., S.J. Taubman, P.D. Brown, M. J. Iacono, S.A. Clough, 1997: Radiative transfer for inhomogeneous atmospheres: RRTM, a validated correlated-k model for the longwave. *J. Geophys. Res.*, **102**, 16663-16682.
- Morrison, H., G. Thompson, V. Tatarskii, 2009: Impact of cloud microphysics on the development of trailing stratiform precipitation in a simulated squall line: Comparison of one- and two-moment schemes. *Mon. Wea. Rev.*, **137**, 991-1007.
- , J.A. Milbrandt, 2011: Comparison of two-moment bulk microphysics schemes in idealized supercell thunderstorm simulations. *Mon. Wea. Rev.*, **139**, 1103-1130.
- Powell, S.W., R.A. Houze, A. Kumar, S.A. McFarlane, 2012, Comparison of simulated and observed continental tropical anvil clouds and their radiative heating profiles. *J. Atmos. Sci.*, **69**, 2662–2681.
- Protat, A., J. Delanoe, D. Bouniol, A. J. Heymsfield, A. Bansemer, and P. Brown, 2007: Evaluation of ice water content retrievals from cloud radar reflectivity and temperature using a large airborne in situ microphysical database. *J. Appl. Met. and Climo.*, **40**, 557-572.
- Randall, D., M. Khairoutdinov, A. Arakawa, W. Gabowski, 2003: Breaking the cloud parameterization deadlock. *Bull. Amer. Meteor. Soc.*, **84**, 1547-1564.

- Reisner, J., Rasmussen, R. M., R. T. Brientjes, 1998: Explicit forecasting of supercooled liquid water in winter storms using the MM5 mesoscale model. *Quart. J. Roy. Meteor. Soc.*, **124**, 1071-1107.
- Rossow, W.B., R.A. Schiffer, 2001: Advances in understanding clouds from ISCCP. *Bull. Amer. Meteor. Soc.*, **80**, 2261-2287.
- Rutledge, S. A., P. V. Hobbs, 1984: The mesoscale and microscale structure and organization of clouds and precipitation in mid-latitude cyclones. Part XII: A diagnostic modelling study of precipitation development in narrow cold-frontal rainbands. *J. Atmos. Sci.*, **41**, 2949-2972.
- Sanderson, B., C. Piani, W. J. Ingram, D. A. Stone, and M. R. Allen, 2008: Towards constraining climate sensitivity by linear analysis of feedback patterns in thousands of perturbed-physics GCM simulations. *Clim. Dyn.*, **30**, 175-190.
- Schmitt, C.G., A.J. Heymsfield, 2009: The size distribution and mass-weighted terminal velocity of low-latitude tropopause cirrus crystal populations. *J. Atmos. Sci.*, **66**, 2013-2028.
- Seifert, A., K. D. Beheng, 2001: A double-moment parameterization for simulating autoconversion, accretion and self-collection. *Atmos. Res.*, **59-60**, 265-281.
- Skamarock, W.C., J.B. Klemp, J. Dudhia, D.O. Gill, D.M. Barker, W. Wang, J.G. Powers, 2007: A description of the Advanced Research WRF Version 2. *NCAR technical note NCAR/TN-468+STR*.
- Smith, W.L., P. Minnis, S.G. Benjamin, S.S. Weygandt, 2010: 4-D cloud water content fields derived from operational satellite data. *IEEE 2010 International Geoscience and Remote Sensing Symposium*, Hawaii.

- Soden, B.J., 2004: The impact of tropical convection and cirrus on upper tropospheric humidity: A lagrangian analysis of satellite measurements. *Geophys. Res. Lett.*, **31**, doi:10.1029/2004GL020980.
- Stephens, G.L., 2005: Cloud feedback in the climate system: A critical review. *J. Climate*, **18**, 237-273.
- Su, H., S.S. Chen, C.S. Bretherton, 1999: Three-dimensional week-long simulations of TOGA COARE convective systems using the MM5 mesoscale model. *J. Atmos. Sci.*, **56**, 2326-2344.
- Sui, C.H., Lau, K.-H., Li, X., 1998. Convective-radiative interaction in simulated diurnal variations of tropical cumulus ensemble. *J. Atmos. Sci.* 54, 637–655. Sun W.-Y., Chang C.-Z., 1986 : Diffusion model for a convective layer. Part I: Numerical simulation of convective boundary layer. *J. Climate Appl. Meteor.*, **25**, 1445-1453.
- Tao, W.-K., J. Simpson, D. Baker, S. Braun, M.-D. Chou, B. Ferrier, D. Johnson, A. Khain, S. Lang, B. Lynn, C.-L. Shie, D. Starr, C.-H. Sui, Y. Wang, P. Wetzel, 2003: Microphysics, radiation and surface processes in the Goddard Cumulus Ensemble (GCE) model. *Meteorol. Atmos. Phys.*, **82**, 97-137.
- Thompson, G., R.M. Rasmussen, K. Manning, 2004: Explicit forecasts of winter precipitation using an improved bulk microphysics scheme. Part I: Description and sensitivity analysis. *Mon. Wea. Rev.*, **132**, 519-542.
- , P.R. Field, R.M. Rasmussen, W.D. Hall, 2008: Explicit forecasts of winter precipitation using an improved bulk microphysics scheme. Part II: Implementation of a new snow parameterization. *Mon. Wea. Rev.*, **136**, 5095-5115.

- Van Weverberg, K., A.M. Vogelmann, H. Morrison, J.A. Milbrandt, 2012a: Sensitivity of idealized squall line simulations to the level of complexity used in two-moment bulk microphysics schemes. *Mon. Wea. Rev.*, **140**, 1883–1907.
- , N.P.M. van Lipzig, L. Delobbe, A.M. Vogelmann, 2012b: The role of precipitation size distributions in km-scale NWP simulations of intense precipitation: Evaluation of cloud properties and surface precipitation. *Quart. J. Roy. Meteor. Soc.*, DOI: 10.1002/qj.1933 (early online release)
- Varble, A., A.M. Fridlind, E.J. Zipser, A.S. Ackerman, J.-P. Chaboureaud, J. Fan, A. Hill, S.A. McFarlane, J.-P. Pinty, B. Shipway, 2011: Evaluation of cloud-resolving model intercomparison simulations using TWP-ICE observations: Precipitation and cloud structure. *J. Geophys. Res.*, **116**, doi:10.1029/2010JD015180.
- Wang, Y., C.N. Long, L.R. Leung, J. Dudhia, S.A. McFarlane, J.H. Mather, S.J. Ghan, X. Liu, 2009: Evaluating regional cloud-permitting simulations of the WRF model for the Tropical Warm Pool International Cloud Experiment (TWP-ICE), Darwin, 2006. *J. Geophys. Res.*, **114**, doi:10.1029/2009JD012729.
- Williams, M., R.A. Houze, 1987: Satellite-observed characteristics of winter monsoon cloud clusters. *Mon. Wea. Rev.*, **115**, 505-519.
- Wright, J.S., R. Fu, A.J. Heymsfield, 2009: A statistical analysis of the influence of deep convection on water vapour variability in the tropical upper troposphere. *Atmos. Chem. Phys.*, **9**, 5847-5864.
- Wu, J., A.D. DelGenio, M.-S. Yao, A.B. Wolf, 2009: WRF and GISS SCM simulations of convective updraft properties during TWP-ICE. *J. Geophys. Res.*, **114**, doi:10.1029/2008JD010851.

- Yuan, J., R.A. Houze Jr., 2010: Global variability of mesoscale convective system anvil structure from A-train satellite data. *J. Climate*, **23**, 5864-5888.
- Yuter, S. E., and R. A. Houze, Jr., 1995: Three-dimensional kinematic and microphysical evolution of Florida cumulonimbus. Part II: Frequency distribution of vertical velocity, reflectivity, and differential reflectivity. *Mon. Wea. Rev.*, **123**, 1941-1963.
- , ———, E.A. Smith, T.T. Wilheit, E. Zipser, 2005: Physical characterization of tropical oceanic convection observed in KWAJEX. *J. Appl. Meteor.*, **44**, 385-415.
- Zhou, Y.P., W.-K. Tao, A.Y. Hou, W.S. Olson, C.-L. Shie, K.-M. Lau, M.-D. Chou, X. Lin, M. Grecu, 2007: Use of high-resolution satellite observations to evaluate cloud and precipitation statistics from cloud-resolving model simulations. Part I: South China sea monsoon experiment. *J. Atmos. Sci.*, **64**, 4309-4329.

7. Figure Captions

- Figure 1: Model domains used for all three simulations over the Tropical Western Pacific (TWP). Successive 20-km and 4-km nested domains are denoted by the inner solid rectangles. The dashed rectangle shows the TWP domain for which GOES-9 satellite data were available. Latitudes and longitudes are indicated by the numbers in the margins. The analysis domain is defined as the common area between the 4-km model domain and the TWP GOES-9 domain.
- Figure 2: Fall speed – diameter (V-D) power-law relations for the precipitating hydrometeor species in the three microphysics schemes, following $V_X = a_{vx} D^{b_{vx}}$, with constants a_{vx} and b_{vx} provided in Table 1. Note that while the x-axis ranges from 0 to 6 mm for rain, snow and graupel, it ranges from 0 to 0.6 mm for cloud ice. MORR and WSM6 have identical rain and snow V-D relations and hence overlay each other. The air density correction is not included.
- Figure 3: Snapshots of the spatial distribution of cloud types at 0325 UTC on 27 December 2003 as observed by GOES-9 (top left) and as simulated by the three microphysics schemes at 0300 UTC the same day. Cloud types (see text) were defined based on the ISCCP classification technique, using CTP and COT and are denoted by the colors as indicated by the legend; land masses are grey. Thick black contours denote those cloud fields identified as MCSs. Latitudes and longitudes are indicated by the numbers in the margins.
- Figure 4: Histograms of the 6-day averaged total area covered within the analysis domain by each of the ISCCP cloud classes (see text) in the observations (GOES) and each of the microphysics experiments. Bars represent the time-averaged coverage of each cloud class and the colors are in accordance with Figure 3. The hatched area denotes the horizontal area of each cloud class that was associated with an MCS.
- Figure 5: Box-and-whisker plots of the size distribution of MCSs as identified in the observations and in each of the microphysics experiments for the entire simulation period and domain. Boxes are limited by the 25th and 75th percentiles of the distribution and whiskers extend out to the 5th and 95th percentiles; the center lines are the medians. Separate statistics are provided for the entire MCS (top), core regions (middle) and anvil regions (bottom), which were defined based on BT as in the definitions of Laing and Fritsch (1993) and determined using the detection-and-spread method used in the cloud-tracking algorithm.
- Figure 6: Vertical profiles of updraft properties, averaged over the entire simulation period and domain for each of the microphysics experiments. Top panels provide total updraft mass-flux (a) and average updraft speed (b) for updrafts associated with MCS core regions only. The bottom panels provide domain-total updraft mass-flux (c) and average updraft speed (d). Updrafts were defined based on a 1 m s^{-1} threshold.
- Figure 7: Vertical profiles of individual updraft characteristics, averaged over the entire simulation time and domain for each of the microphysics experiments. Provided are the average size of *individual* updrafts (a), the number of individual updrafts (b), and the total area covered by *all* updrafts (c). Updrafts were defined based on a 1 m s^{-1} threshold.
- Figure 8: Contoured frequency by altitude diagrams (CFADs) of mixing ratio (q_X) for all three microphysics experiments and for the four precipitating hydrometeor species. Aggregation was done for all hourly output times and the entire analysis domain. The color scale provides the frequency of occurrence with values increasing logarithmically from 1 (blue) to 10^6 (red) for all panels. Note the different ranges of the abscissa.

Figure 9: As in Figure 8, but for the volume-weighted mean diameter (D_X). The abrupt cutoffs in MORR and THOM are caused by size thresholds imposed in these schemes, as mentioned in the text.

Figure 10: As in Figure 8, but for number concentration (N_X).

Figure 11: As in Figure 8, but for the bulk fall velocity (V_X), which was calculated from Eq. 3 and included the density correction.

Figure 12: Probability density functions of snow mixing ratio (q_S) versus snow fall velocity (V_S) in WSM6, MORR, MORR_SS and THOM, based on simulated snow properties of all domain grid cells that are above 10 km. The banded features in WSM6 and THOM are caused by the temperature dependency of the N_{OS} parameter and hence reflect the different model levels.

Figure 13: Vertical-latitudinal cross sections through the most northeastern MCS depicted in Figure 3 for WSM6 (top), MORR (middle) and THOM (bottom). For each experiment, the cross sections were taken across the 25 strongest MCS updrafts. All cross sections were subsequently centered on the main updraft and averaged into the cross sections shown. The left hand panels show the dynamic features of the MCSs. Colored shading indicates the deviation of wind speed from the average wind speed at each level. Shading is in red if the deviation of the wind speed is directed towards the main updraft (in the center of the panel, at 800 km, i.e. convergence). Shading is in blue if the deviation of the wind speed is directed away from the updraft in the center (i.e. divergence). Arrows indicate the deviation of wind vectors from the panel-averaged wind vector. The largest arrows correspond to about 10 m s^{-1} . Contours on the left hand panels depict the snow sedimentation velocities (solid contours are drawn every 0.3 m s^{-1}) and ice sedimentation velocities (dashed contours drawn every 0.3 m s^{-1}). The extinction coefficient is shown on the right hand panels as grey shading. Contours on these panels are the relative humidity with respect to ice (contours drawn every 10% from 75% to 95%).

Figure 14: Time and domain average vertical profiles of divergence/convergence associated with mid-level updrafts (vertical velocity exceeding 1 m s^{-1} between 5 and 10 km altitude) for the three microphysics schemes. Negative values indicate convergence, positive values indicate divergence.

Figure 15: Spatial distribution of 6-day surface precipitation accumulations as observed by GPCP and as simulated by all microphysics schemes. Observations have a grid spacing of $1^\circ \times 1^\circ$ and simulated precipitation fields were aggregated from the original 4 km grid spacing to the observed grid spacing for comparison. Latitudes and longitudes are indicated by the numbers in the margins.

Figure 16: Vertical profiles of rain properties in all three microphysics schemes, associated with (left) areas with significant rainfall (surface rain rates exceeding 1 mm hr^{-1}) and (right) associated with the most intense precipitation areas (surface rain rates exceeding 50 mm hr^{-1}), averaged over the domain and entire simulation period. Depicted are (top) the rain mixing ratio (q_R), (middle) volume mean drop diameter (D_R), and (bottom) the relative humidity (RH).

Table 1: Overview of the primary differences in terms of particle size distributions between the three cloud microphysics schemes investigated in this study. Given are the shape of the distribution (negative exponential or gamma), the intercept (N_{0X}), constants a_{mx} and b_{mx} for the mass-diameter relations, constants a_{vx} and b_{vx} for the velocity-diameter relations, and the particle density (ρ_x). References for each of the variables are provided below the table.

Scheme	Species	Shape	$N_{0X} \text{ (m}^{-1}\text{)}$	$a_{mx} \text{ (kg m}^{-b_{mx}}\text{)}$	b_{mx}	$a_{vx} \text{ (m}^{s-1} \text{ m}^{-b_{vx}}\text{)}$	b_{vx}	$\rho_x \text{ (kg m}^{-3}\text{)}$
WSM6	Rain	EXP	8×10^6	$\frac{\pi \rho_r}{6}$	3.	841.9^*	0.8^*	1000.
	Snow	EXP	$\min[2 \times 10^8, 2 \times 10^6 \times \exp[0.12(T_0 - T)]]^\S$	$\frac{\pi \rho_s}{6}$	3.	11.72^\P	0.41^\P	100.
	Graupel	EXP	4×10^6	$\frac{\pi \rho_g}{6}$	3.	$330.^\P$	0.8^\P	500.
	Ice ¹	EXP	-	-	-	-	-	-
THOM	Rain	EXP	$\left(\frac{N_1 - N_2}{2}\right) \tanh\left[\frac{(q_{r0} - q_r)}{4q_{r0}}\right] + \frac{N_1 + N_2}{2}^\S$	$\frac{\pi \rho_r}{6}$	3.	$4854.4^{@,2}$	$1.^{@,2}$	1000.
	Snow	EXP+GAM	$\min[2 \times 10^8, 2 \times 10^6 \times \exp[0.12(T_0 - T)]]^\S$	$0.069^\£$	$2.^\£$	$40.^{\S,2}$	$0.55^{\S,2}$	100.
	Graupel	EXP	$\max\left[10^4, \min\left(\frac{200}{q_g}, 5 \times 10^6\right)\right]^\S$	$\frac{\pi \rho_g}{6}$	3.	$442.^\dagger$	0.89^\dagger	400.
	Ice	EXP	PROGNOSTIC	$\frac{\pi \rho_i}{6}$	3.	1847.5^\S	$1.^\S$	890.
MORR	Rain	EXP	PROGNOSTIC	$\frac{\pi \rho_r}{6}$	3.	841.9^*	0.8^*	1000.
	Snow	EXP	PROGNOSTIC	$\frac{\pi \rho_s}{6}$	3.	11.72^\P	0.41^\P	100.
	Graupel	EXP	PROGNOSTIC	$\frac{\pi \rho_g}{6}$	3.	$19.3^\#$	$0.37^\#$	400.
	Ice	EXP	PROGNOSTIC	$\frac{\pi \rho_i}{6}$	3.	$700.^\&$	$1.^\&$	500.

¹ N_i in WSM6 is derived as a function of q_i : $N_i = c(\rho q_i)^d$ where c and d are constants. V_i is also a function of q_i , following Heymsfield and Donner (1990)

² V_s and V_r in THOM follow Ferrier (1994) and are given by $V_x = a_{vx} D^{b_{vx}} \exp(-fD)$, where f is 195 and 125 for rain and snow respectively

* Liu and Orville (1969)

[†] Locatelli and Hobbs (1974)

[@] Ferrier 1994

[§] Thompson et al. (2008)

[†] Heymsfield and Kajikawa (1987)

[#] Ferrier et al. (1995)

[&] Morrison et al. (2009)

[£] Cox (1988)

[§] Houze et al. (1979)

Table 2: Cloud fractions of the analysis domain (see Fig. 1) occupied by high clouds, middle clouds and low clouds in the observations and the model simulations. Cloud fractions were averaged over all output times (hourly), provided that the solar zenith angle was less than 70°. Cloud fraction for the domain are given (bold numbers), as well as the fraction of the total that are within the MCSs. The last column lists the total cloud fraction (bold) and the total MCS fraction for the entire domain.

	High Clouds (%)		Middle Clouds (%)		Low Clouds (%)		Total (%)	
	Total	MCS	Total	MCS	Total	MCS	Total	MCS
GOES	35	96	4	4	2	0	41	17
WSM6	12	78	6	14	10	8	28	3
MORR	34	92	5	6	6	2	45	28
MORR_SS	36	91	5	7	5	2	46	33
THOM	31	92	3	5	5	3	39	19

Table 3: Statistics of the MCSs tracked in the observations and the simulations for the analysis domain and simulation period. Provided are the total number of individual MCS tracks, as well as the average longevity for each track. The average size, BT, COT and CTP are given for the MCSs and also separately for the MCS core and anvil regions, based on the Laing and Fritsch (1993) definitions and determined using the detection-and-spread method used in the cloud-tracking algorithm. Pearson correlation coefficients are provided between the simulated and the observed MCS size time series in parentheses.

	# Tracks	Size (10^5 km^2)			BT (K)		
		Core	Anvil	Total (Correlation)	Core	Anvil	Total
GOES	31	1.6	7.1	8.7	210	246	238
WSM6	18	0.7	4.8	5.6 (0.54)	215	237	233
MORR	15	3.0	11.2	14.2 (0.44)	215	238	232
MORR_SS	18	5.0	14.4	19.4 (0.33)	214	238	231
THOM	30	2.6	8.6	11.2 (0.42)	214	239	232
	Longevity (hours)	COT			CTP (hPa)		
GOES	21	26.9	8.6	12.6	162	256	235
WSM6	19	26.1	19.0	20.3	208	370	341
MORR	32	23.4	15.6	17.4	131	201	184
MORR_SS	23	22.8	15.3	17.5	131	209	185
THOM	24	29.8	12.2	17.1	129	231	203

Table 4: Mean 6-day surface precipitation accumulations (SP), averaged over the entire analysis domain as observed (GPCP and TRMM) and as simulated by each experiment. The simulated and TRMM precipitation amounts were aggregated to the GPCP $1^\circ \times 1^\circ$ grid for comparison. For the simulations the bias and Root Mean Square Error (RMSE) of the 6-day precipitation accumulations are also provided, which were calculated using the GPCP precipitation as ground truth. Further, the maximum accumulation as well as the time-averaged domain peak precipitation rate is provided. The last column provides the fractional coverage of surface precipitation for the entire domain for only grid cells that have precipitation accumulations of more than 10 mm.

	Mean SP (mm)	Bias (mm)	RMSE (mm)	Maximum SP (mm)	Mean Peak Rate (mm hr ⁻¹)	Coverage (%)
GPCP	51.7	-	-	213	-	79.1
TRMM	54.5	-	-	334	-	82.2
WSM6	73.8	22.1	59.6	295	249	90.2
MORR	72.9	21.1	60.2	483	172	88.5
THOM	73.1	21.4	57.9	376	238	87.9

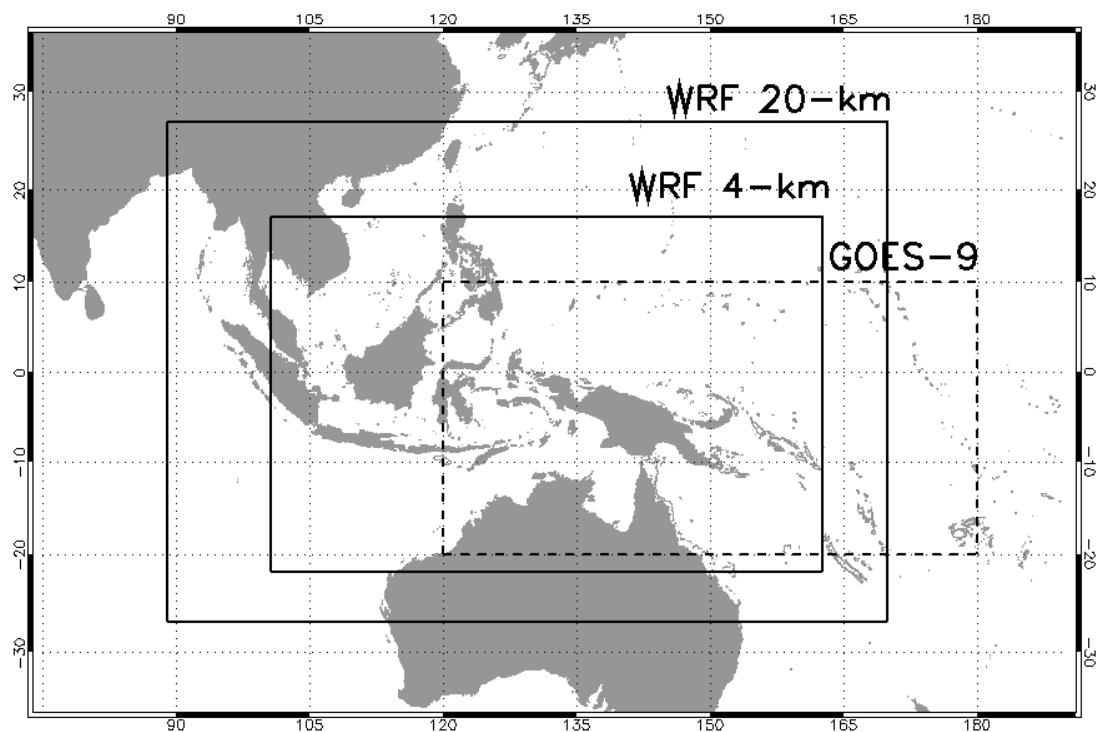


Figure 1: Model domains used for all three simulations over the Tropical Western Pacific (TWP). Successive 20-km and 4-km nested domains are denoted by the inner solid rectangles. The dashed rectangle shows the TWP domain for which GOES-9 satellite data were available. Latitudes and longitudes are indicated by the numbers in the margins. The analysis domain is defined as the common area between the 4-km model domain and the TWP GOES-9 domain.

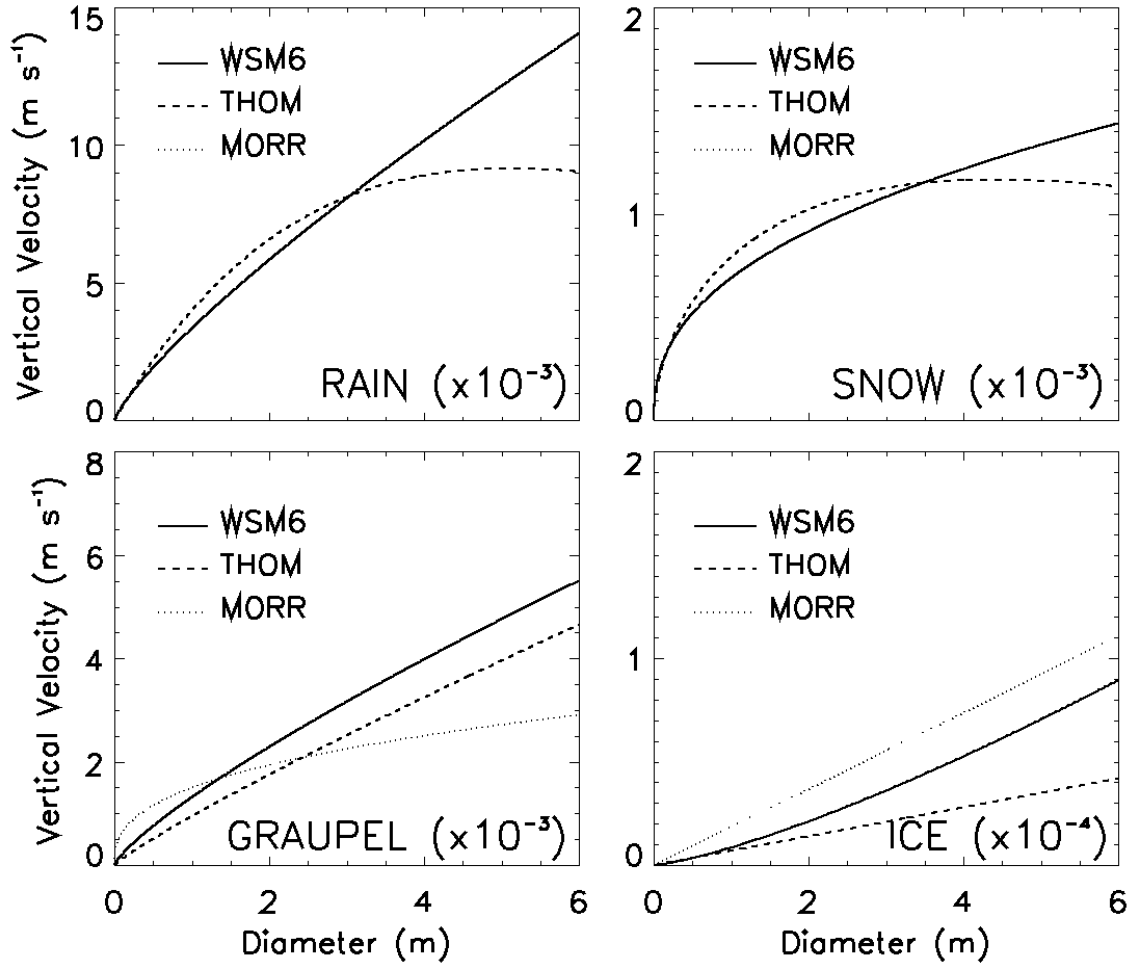


Figure 2: Fall speed – diameter (V-D) power-law relations for the precipitating hydrometeor species in the three microphysics schemes, following $V_X = a_{vx} D^{b_{vx}}$, with constants a_{vx} and b_{vx} provided in Table 1. Note that while the x-axis ranges from 0 to 6 mm for rain, snow and graupel, it ranges from 0 to 0.6 mm for cloud ice. MORR and WSM6 have identical rain and snow V-D relations and hence overlay each other. The air density correction is not included.

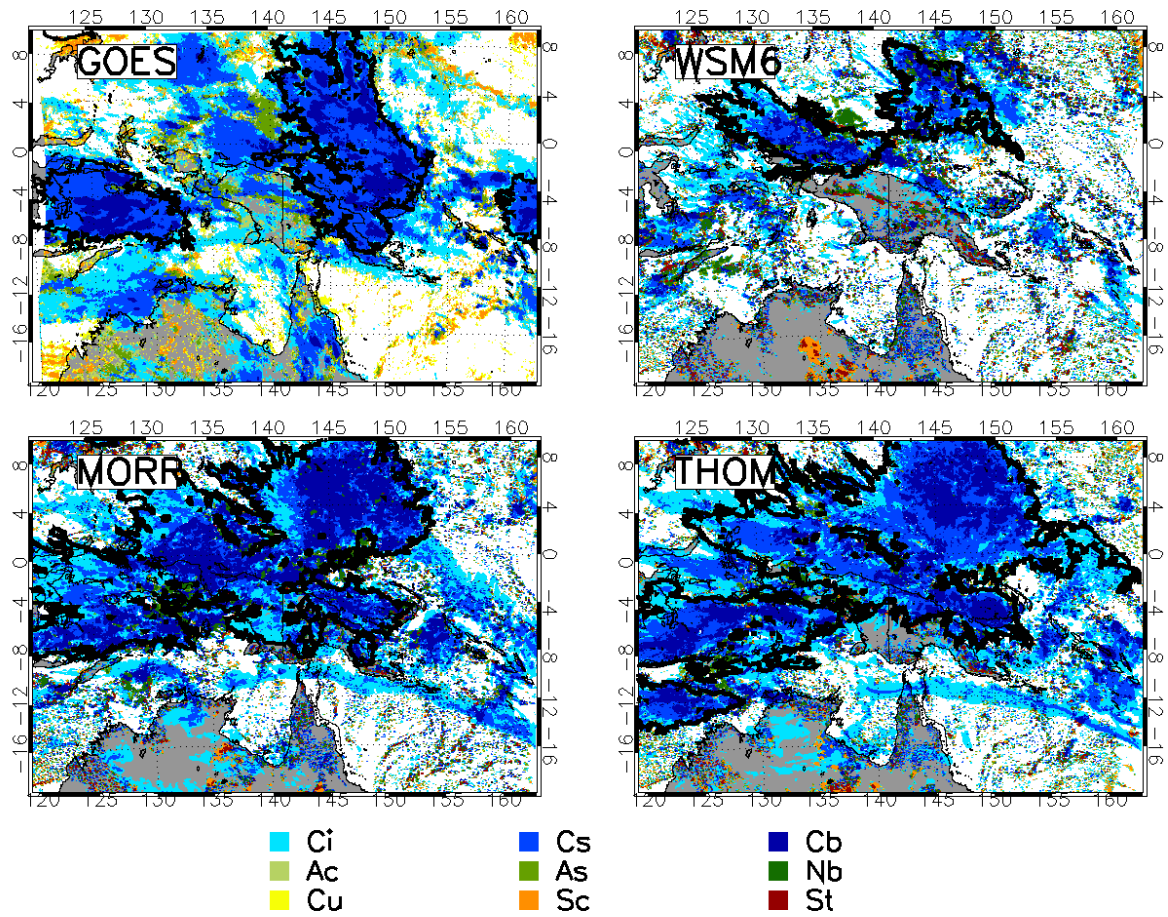


Figure 3: Snapshots of the spatial distribution of cloud types at 0325 UTC on 27 December 2003 as observed by GOES-9 (top left) and as simulated by the three microphysics schemes at 0300 UTC the same day. Cloud types (see text) were defined based on the ISCCP classification technique, using CTP and COT and are denoted by the colors as indicated by the legend; land masses are grey. Thick black contours denote those cloud fields identified as MCSs. Latitudes and longitudes are indicated by the numbers in the margins.

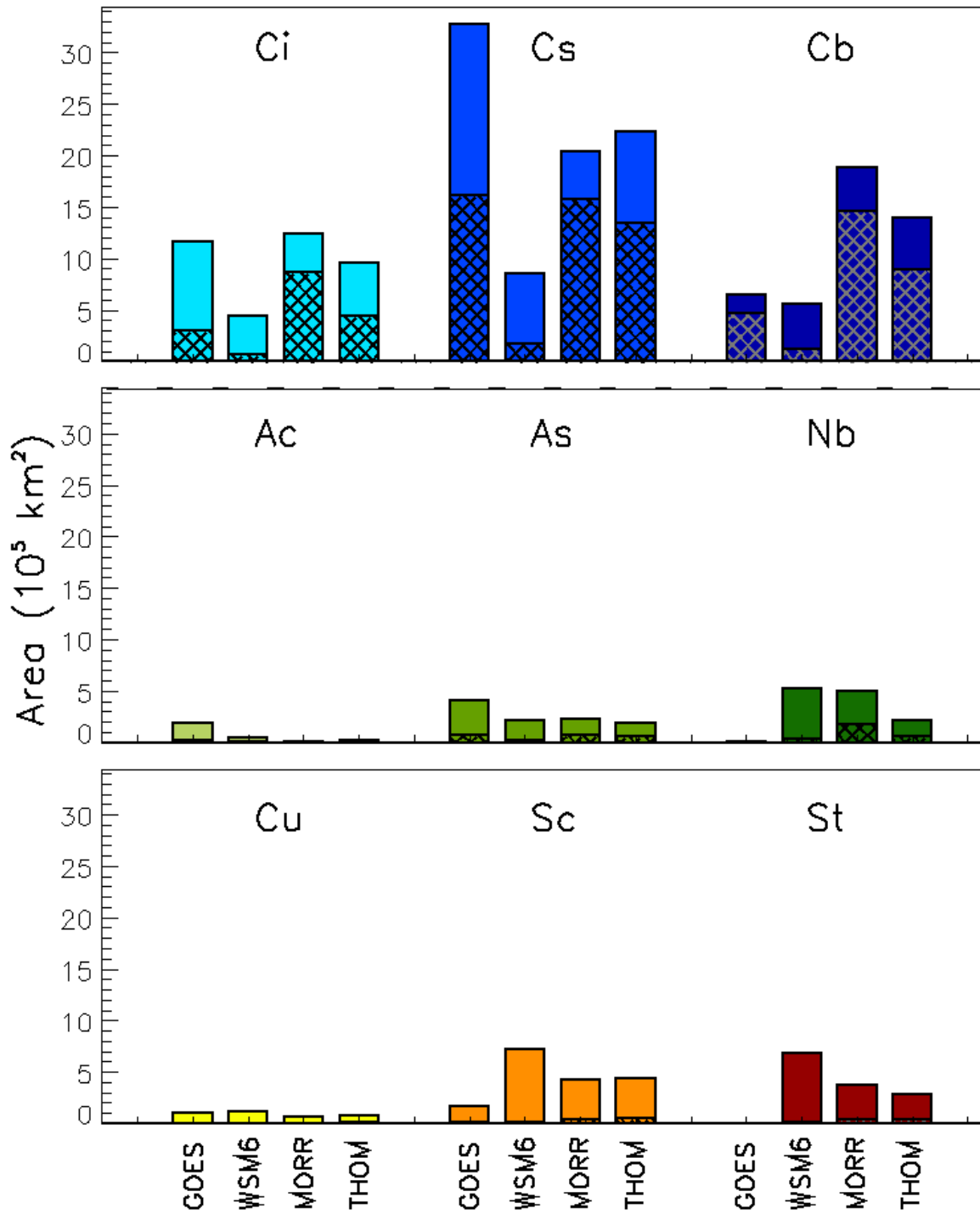


Figure 4: Histograms of the 6-day averaged total area covered within the analysis domain by each of the ISCCP cloud classes (see text) in the observations (GOES) and each of the microphysics experiments. Bars represent the time-averaged coverage of each cloud class and the colors are in accordance with Figure 3. The hatched area denotes the horizontal area of each cloud class that was associated with an MCS.

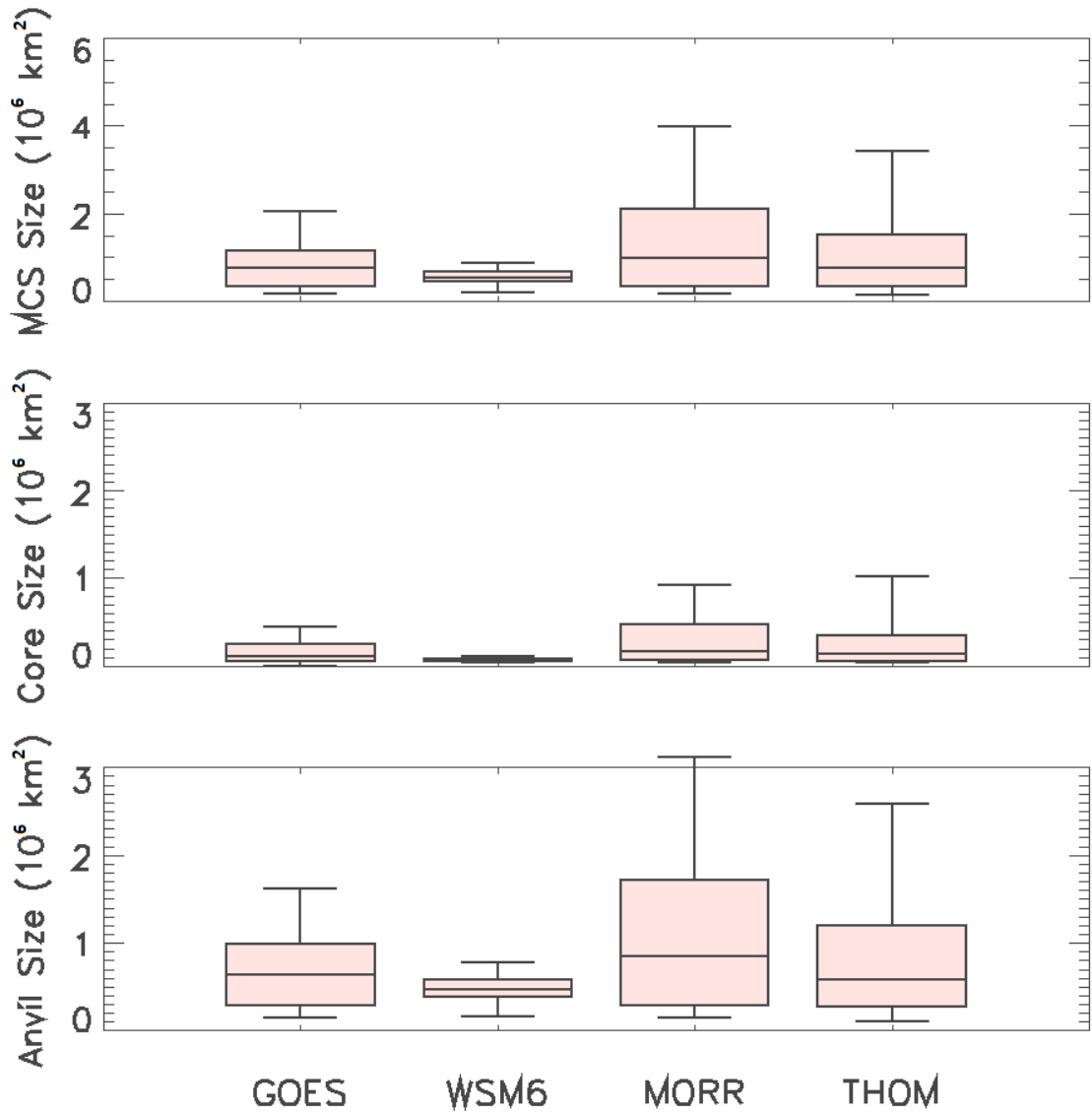


Figure 5: Box-and-whisker plots of the size distribution of MCSs as identified in the observations and in each of the microphysics experiments for the entire simulation period and domain. Boxes are limited by the 25th and 75th percentiles of the distribution and whiskers extend out to the 5th and 95th percentiles; the center lines are the medians. Separate statistics are provided for the entire MCS (top), core regions (middle) and anvil regions (bottom), which were defined based on BT as in the definitions of Laing and Fritsch (1993) and determined using the detection-and-spread method used in the cloud-tracking algorithm.

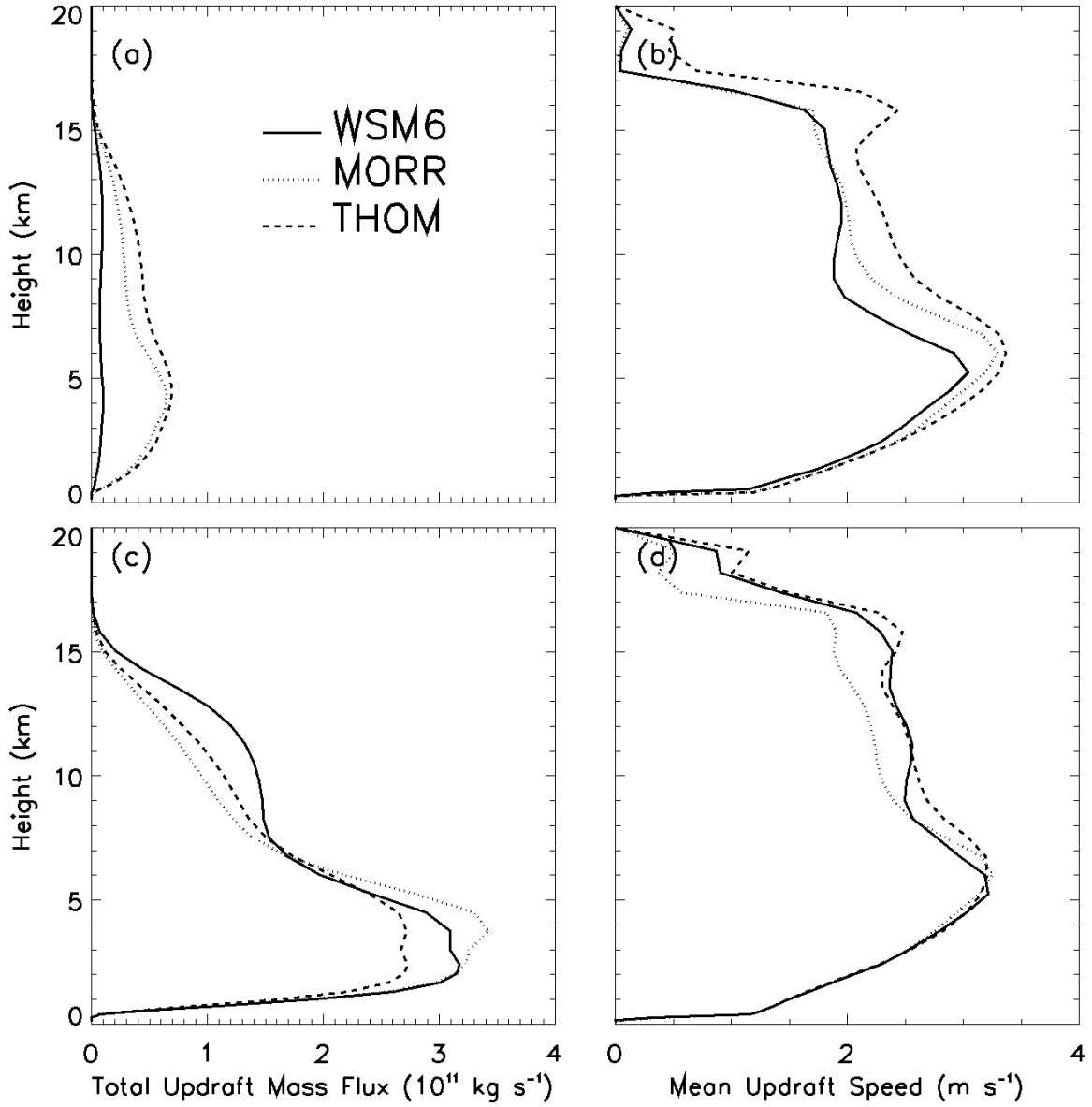


Figure 6: Vertical profiles of updraft properties, averaged over the entire simulation period and domain for each of the microphysics experiments. Top panels provide total updraft mass-flux (a) and average updraft speed (b) for updrafts associated with MCS core regions only. The bottom panels provide domain-total updraft mass-flux (c) and average updraft speed (d). Updrafts were defined based on a 1 m s^{-1} threshold.

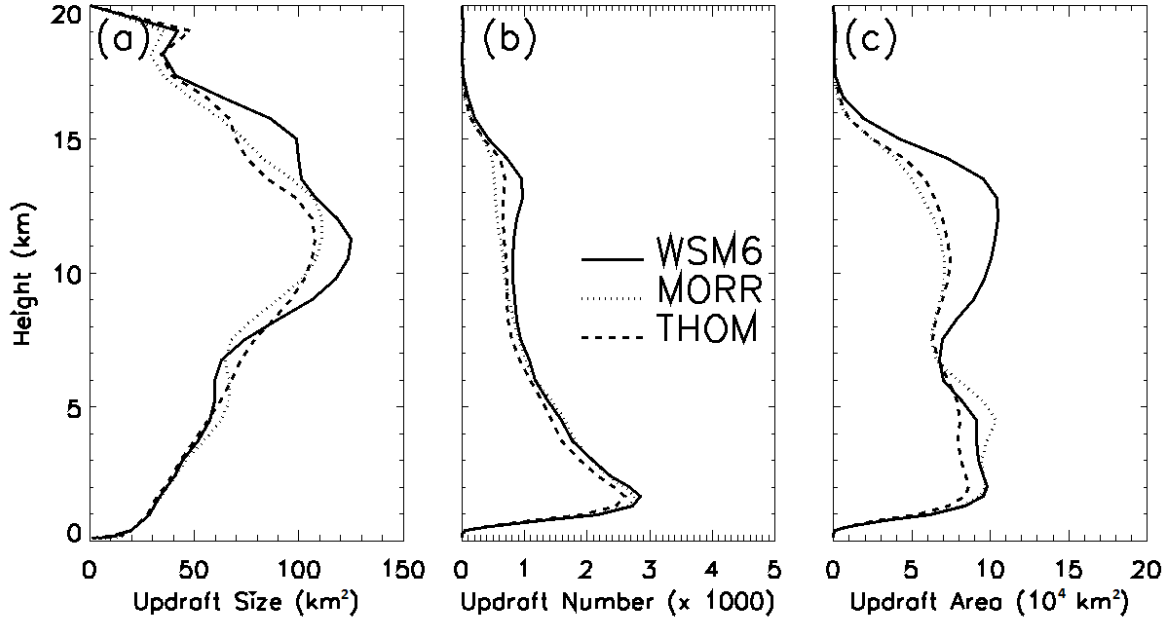


Figure 7: Vertical profiles of individual updraft characteristics, averaged over the entire simulation time and domain for each of the microphysics experiments. Provided are the average size of *individual* updrafts (a), the number of individual updrafts (b), and the total area covered by *all* updrafts (c). Updrafts were defined based on a 1 m s^{-1} threshold.

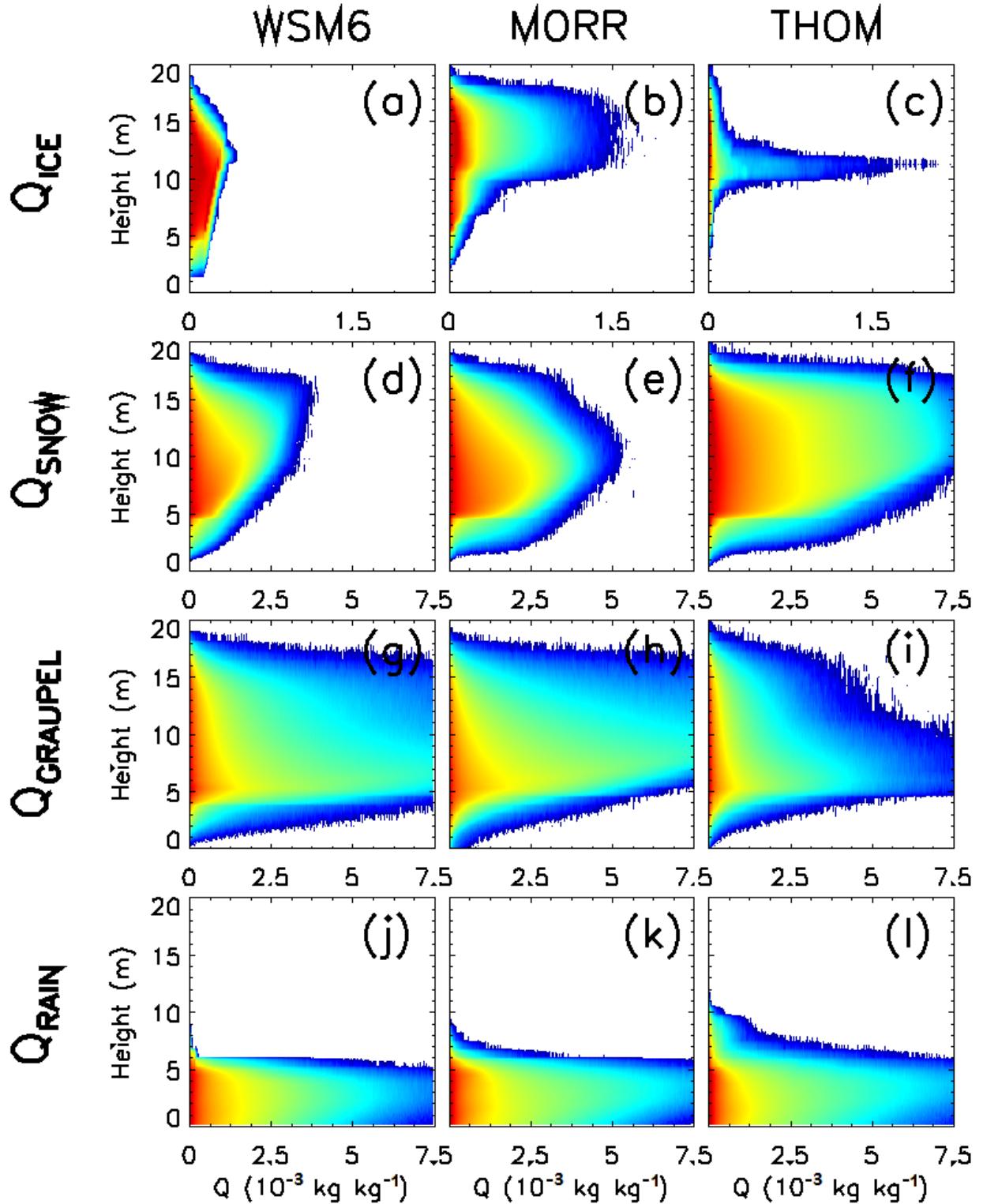


Figure 8: Contoured frequency by altitude diagrams (CFADs) of mixing ratio (q_x) for all three microphysics experiments and for the four precipitating hydrometeor species. Aggregation was done for all hourly output times and the entire analysis domain. The color scale provides the frequency of occurrence with values increasing logarithmically from 1 (blue) to 10^6 (red) for all panels. Note the different ranges of the abscissa.

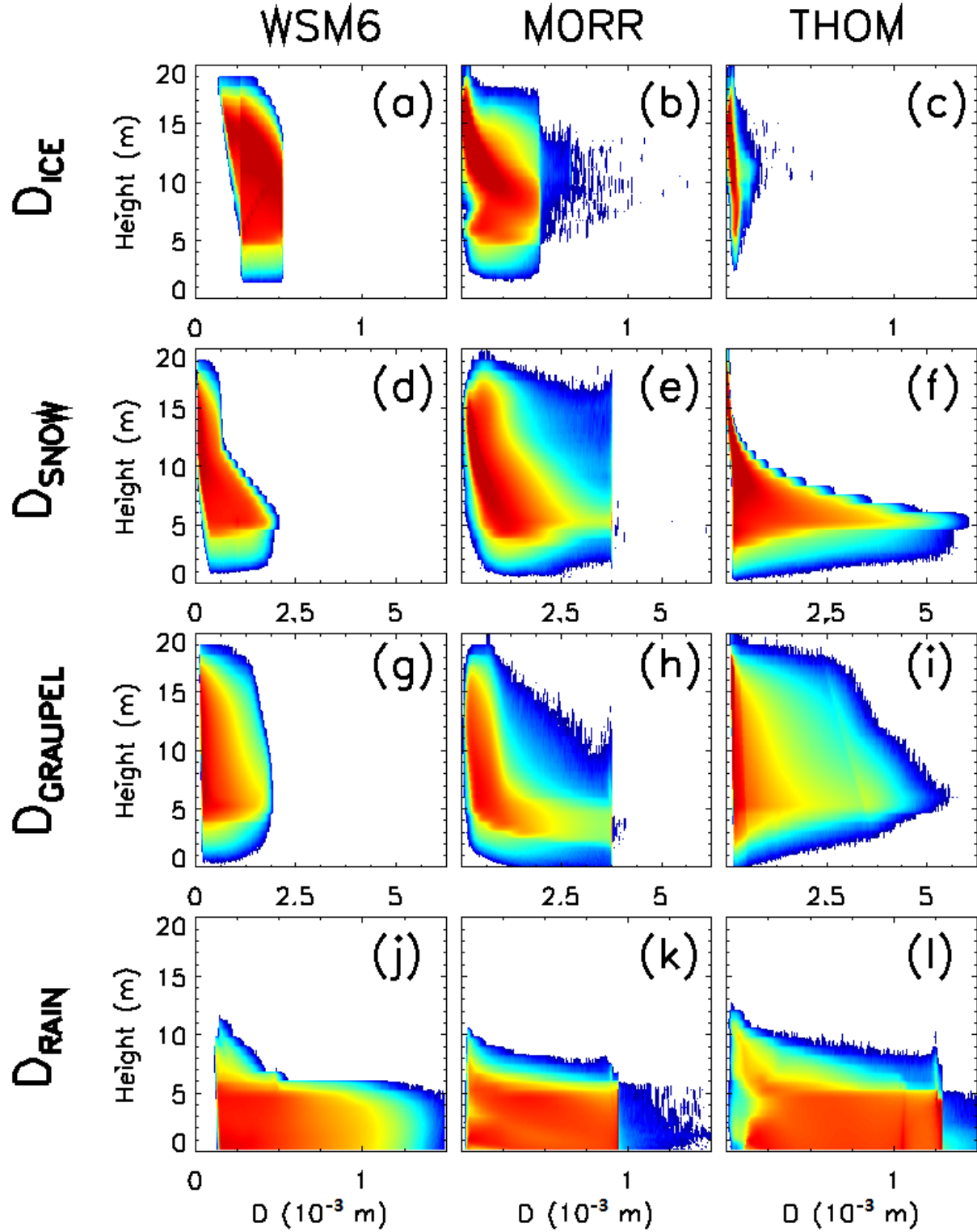


Figure 9: As in Figure 8, but for the volume-weighted mean diameter (D_X). The abrupt cutoffs in MORR and THOM are caused by size thresholds imposed in these schemes, as mentioned in the text.

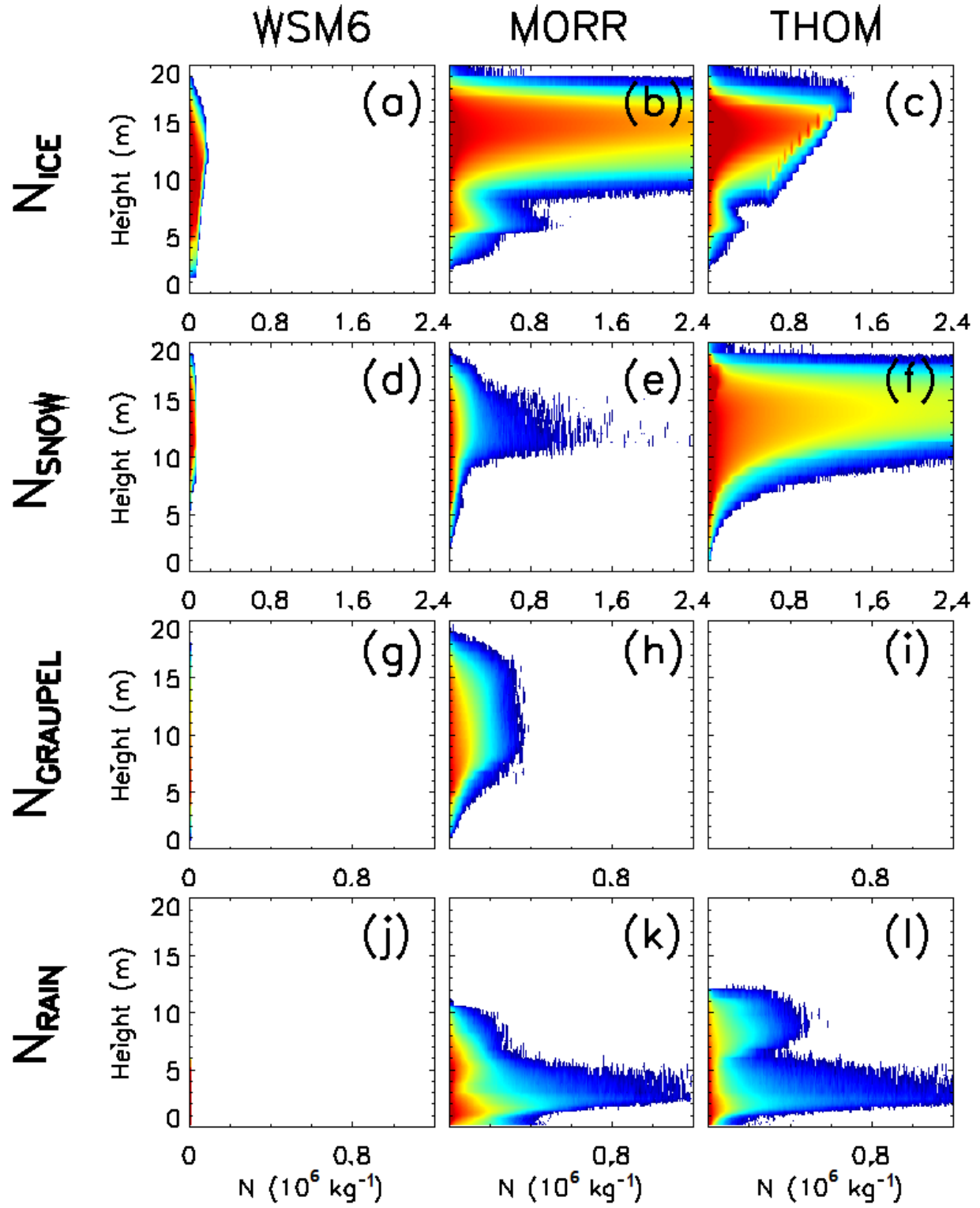


Figure 10: As in Figure 8, but for number concentration (N_X).

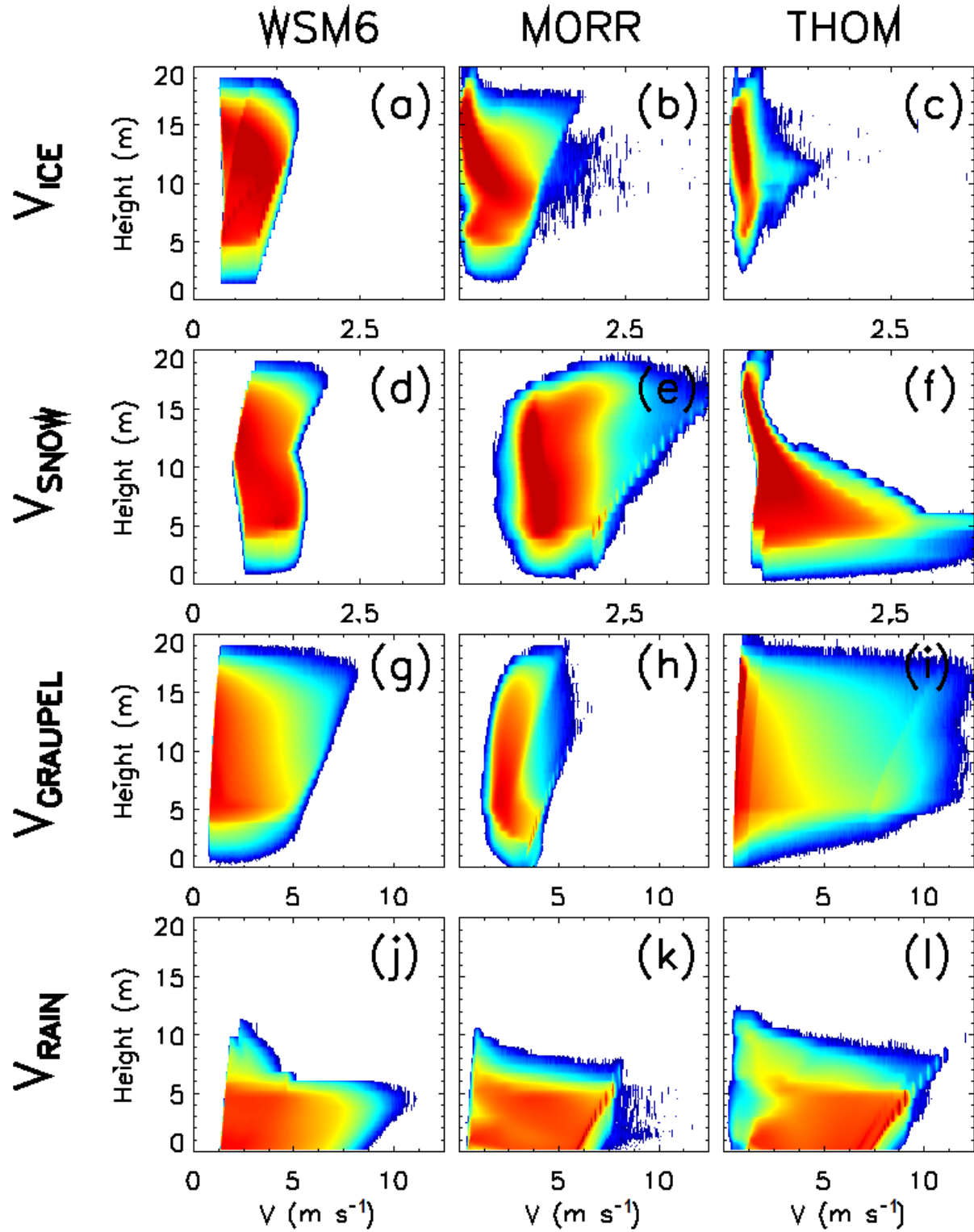


Figure 11: As in Figure 8, but for the bulk fall velocity (V_X), which was calculated from Eq. 3 and included the density correction.

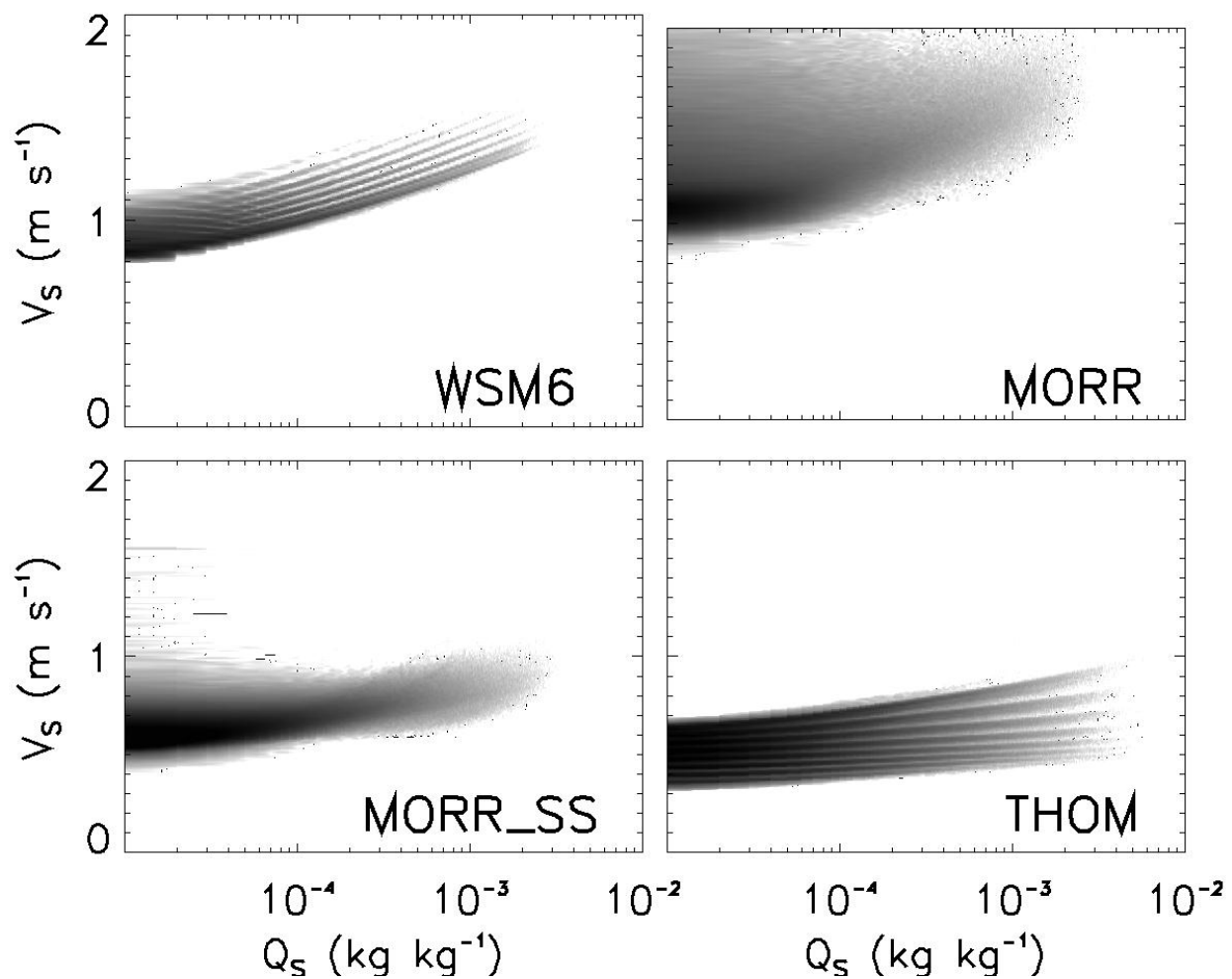


Figure 12: Probability density functions of snow mixing ratio (q_s) versus snow fall velocity (V_s) in WSM6, MORR, MORR_SS and THOM, based on simulated snow properties of all domain grid cells that are above 10 km. The banded features in WSM6 and THOM are caused by the temperature dependency of the N_{os} parameter and hence reflect the different model levels.

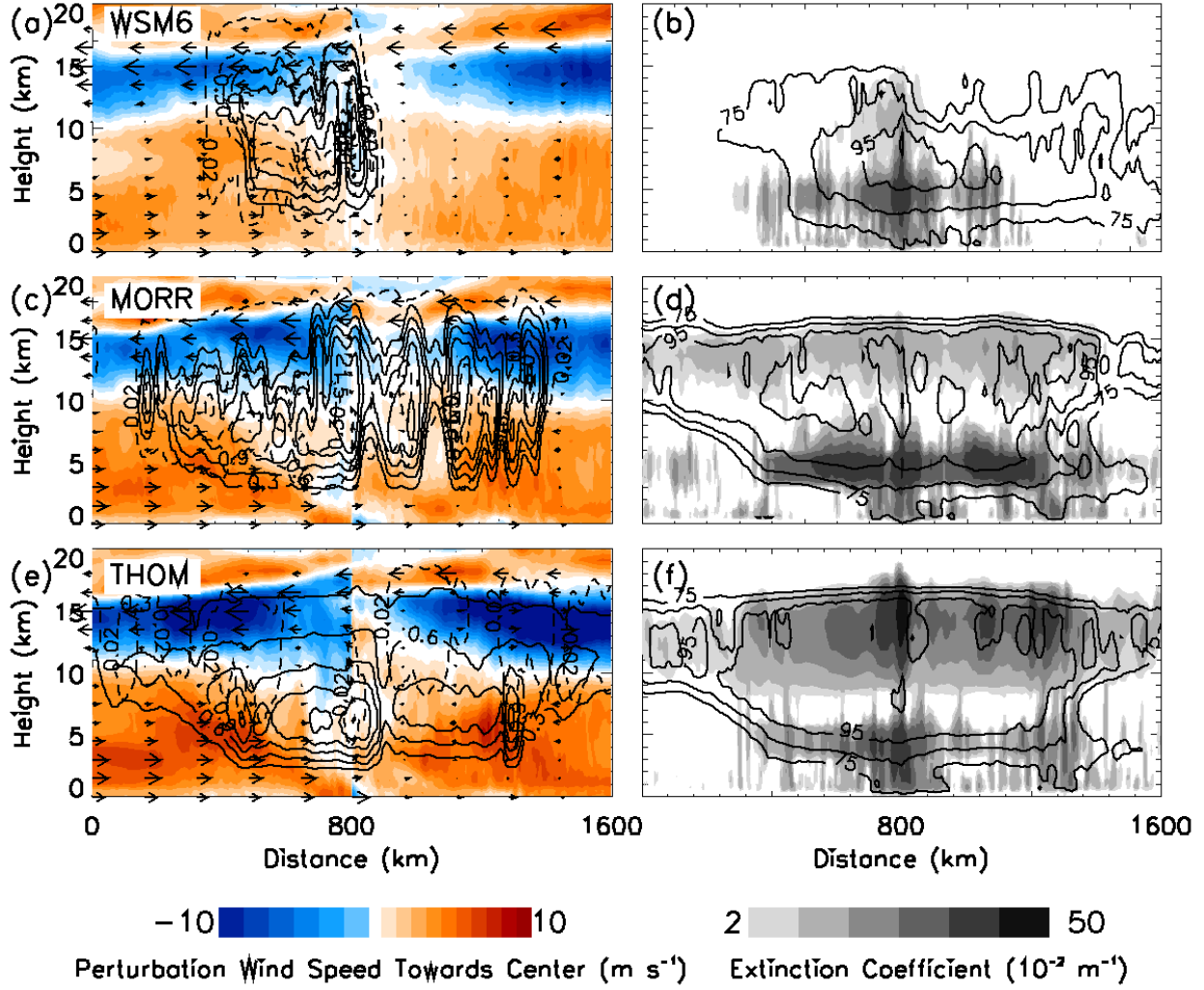


Figure 13: Vertical-latitude cross sections through the most northeastern MCS depicted in Figure 3 for WSM6 (top), MORR (middle) and THOM (bottom). For each experiment, the cross sections were taken across the 25 strongest MCS updrafts. All cross sections were subsequently centered on the main updraft and averaged into the cross sections shown. The left hand panels show the dynamic features of the MCSs. Colored shading indicates the deviation of wind speed from the average wind speed at each level. Shading is in red if the deviation of the wind speed is directed towards the main updraft (in the center of the panel, at 800 km, i.e. convergence). Shading is in blue if the deviation of the wind speed is directed away from the updraft in the center (i.e. divergence). Arrows indicate the deviation of wind vectors from the panel-averaged wind vector. The largest arrows correspond to about 10 m s^{-1} . Contours on the left hand panels depict the snow sedimentation velocities (solid contours are drawn every 0.3 m s^{-1}) and ice sedimentation velocities (dashed contours drawn every 0.3 m s^{-1}). The extinction coefficient is shown on the right hand panels as grey shading. Contours on these panels are the relative humidity with respect to ice (contours drawn every 10% from 75% to 95%).

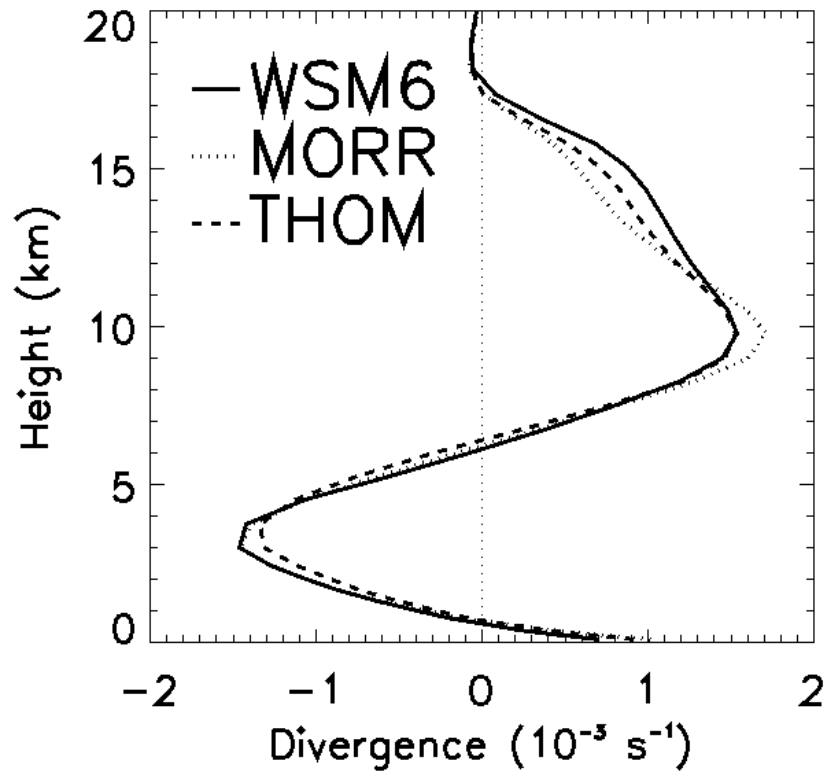


Figure 14: Time and domain average vertical profiles of divergence/convergence associated with mid-level updrafts (vertical velocity exceeding 1 m s^{-1} between 5 and 10 km altitude) for the three microphysics schemes. Negative values indicate convergence, positive values indicate divergence.

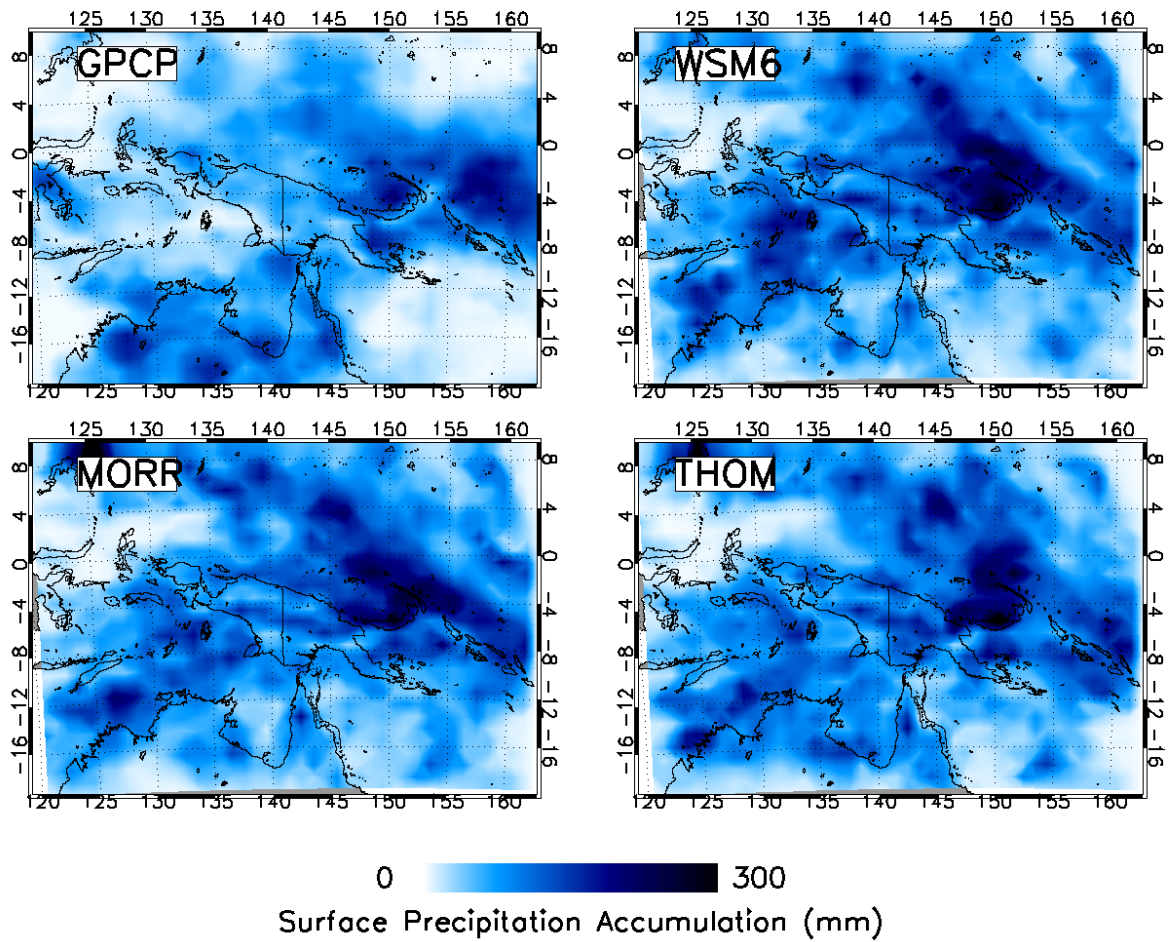


Figure 15: Spatial distribution of 6-day surface precipitation accumulations as observed by GPCP and as simulated by all microphysics schemes. Observations have a grid spacing of $1^\circ \times 1^\circ$ and simulated precipitation fields were aggregated from the original 4 km grid spacing to the observed grid spacing for comparison. Latitudes and longitudes are indicated by the numbers in the margins.

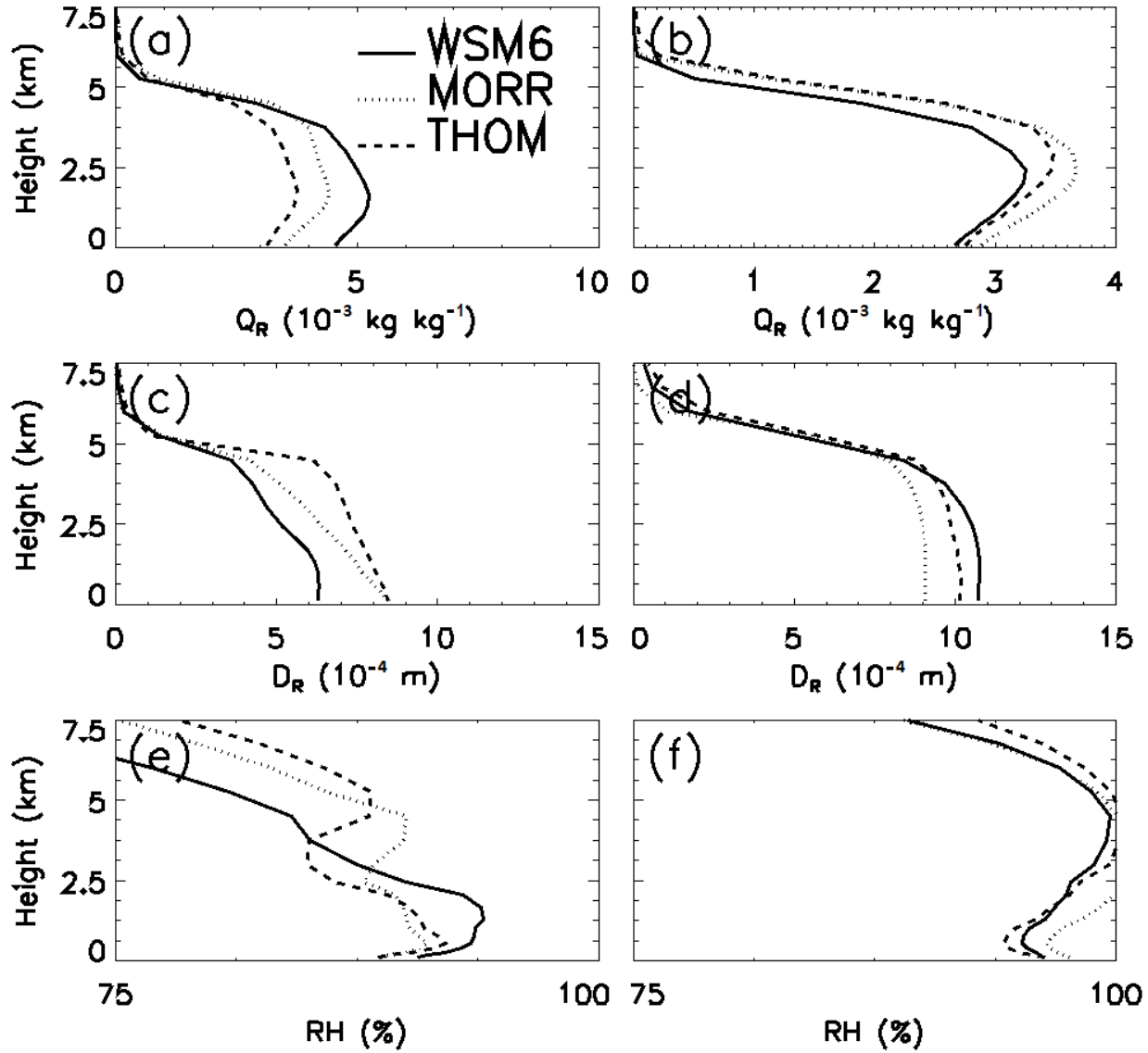


Figure 16: Vertical profiles of rain properties in all three microphysics schemes, associated with (left) areas with significant rainfall (surface rain rates exceeding 1 mm hr^{-1}) and (right) associated with the most intense precipitation areas (surface rain rates exceeding 50 mm hr^{-1}), averaged over the domain and entire simulation period. Depicted are (top) the rain mixing ratio (q_R), (middle) volume mean drop diameter (D_R), and (bottom) the relative humidity (RH).